






# Pol-InSAR and PolSAR based Inversion Modelling for Snow Depth and SWE Estimation in the Northwestern Himalayan Watershed

 Sayantan Majumdar<sup>a,b,\*</sup>,  Praveen K. Thakur<sup>b</sup>,  Ling Chang<sup>a</sup>,  
 Shashi Kumar<sup>b</sup>,  Sneh Mani<sup>c</sup>

<sup>a</sup>*Faculty of Geo-information Science and Earth Observation (ITC), University of Twente*

<sup>b</sup>*Indian Institute of Remote Sensing (IIRS), ISRO*

<sup>c</sup>*Snow and Avalanche Study Establishment (SASE), DRDO*


---

## Abstract

Snow depth (SD) and Snow Water Equivalent (SWE) constitute essential physical properties of snow and find extensive usage in the hydrological modelling domain. However, the prominent impact of the hydrometeorological conditions and difficult terrain conditions inhibit accurate measurement of the SD and SWE— an ongoing research problem in the cryosphere paradigm. In this context, spaceborne synthetic aperture radar (SAR) systems benefit from global coverage at sufficiently high spatial resolutions. The copolar phase difference (CPD) method based on the X-band polarimetric SAR (PolSAR) technique has displayed promising results regarding the fresh snow depth (FSD) estimation in the literature. Still, this FSD inversion model has not been tested in the presence of extreme topographically varying conditions, such as the northwestern Himalayan belt. It is also susceptible to high volume scattering at X-band occurring from the increased snow grain sizes as a result of the standing (or old) snow formation driven by the temperature induced snow metamorphosis process. Hence, to model this volume decorrelation, the polarimetric SAR interferometry (Pol-InSAR) technique can be applied. In this work, the FSD and standing snow depth (SSD) are computed using the

---

\*Corresponding author

Email address: [ir.sayantan.majumdar@gmail.com](mailto:ir.sayantan.majumdar@gmail.com) ( Sayantan Majumdar)

PolSAR CPD method and the single-baseline Pol-InSAR based hybrid Digital Elevation Model (DEM) differencing and coherence amplitude inversion model. To achieve these, the TerraSAR-X, TanDEM-X Coregistered Single look Slant range Complex (CoSSC) bistatic acquisition over Dhundi (situated in the Beas watershed, northwestern Himalayas, India) on January 8, 2016, is used. Due to the associated problems of model parameter tuning, complex topographical conditions, and limited ground-truth measurements, appropriate sensitivity analyses have been carried out for the parameter optimisation. Furthermore, the uncertainty sources are identified by performing a summer (June 8, 2017) and wintertime (January 8, 2016) comparative analysis of the study area which quantitatively highlights the changes in the percentages of the surface and volume scatterings. Evidently, the improved models display sufficiently high FSD and SSD accuracies of 94.83% and 99.53% respectively with the corresponding fresh SWE (FSWE) and standing SWE (SSWE) accuracies of 94.84% and 99.48% (measured using a  $3 \times 3$  window at Dhundi). These results demonstrate the practicability of the PolSAR and Pol-InSAR models in the context of the SD estimation over rugged terrains.

*Keywords:* Synthetic Aperture Radar, Copolar Phase Difference, Pol-InSAR, Snow Physical Properties, Sensitivity Analysis

---

## 1. Introduction

Snow depth (SD) and snow water equivalent (SWE) are two of the most important physical properties of snow and are extensively used in hydrological models that relate to snowmelt runoff and snow avalanche predictions (Thakur et al., 2017). While snow depth or snow height refers to the distance of the ground to the snow surface, SWE quantifies the amount of water present in a snowpack (layered snow formed by accumulation over time). Theoretically, SWE is defined as the product of snow depth and snow density and can be conceptualised as the amount of liquid water obtained owing to the instantaneous melting of an entire snowpack (Tedesco, 2015). Obtaining

11 accurate estimation of the SD and SWE is quite challenging depending upon the  
12 data availability, variety, and quality, parameterisation method, mathematical  
13 model selection, and the hydrometeorological conditions. Hence, it is considered  
14 to be an important research element in the cryosphere paradigm (Leinss et al.,  
15 2014, 2015, 2016; Conde et al., 2019).

16 Due to the difficulties posed by in-situ or ground based measurements of  
17 the SD and SWE in rugged terrains, remote sensing techniques coupled with  
18 adequately sampled (both in space and time domains) ground measurements  
19 are widely used to improve the quality of these estimated parameters over  
20 considerably large areas (Takala et al., 2011). Currently, LiDAR (Light  
21 Detection and Ranging) and spaceborne SAR (Synthetic Aperture Radar) are  
22 the most popular techniques used in the studies related to snow, ice and the  
23 cryosphere in general (Deems et al., 2013; Leinss et al., 2014; Tedesco, 2015).  
24 However, LiDAR can only be used to determine the height of the snow and  
25 cannot be used for measuring other physical properties such as snow density and  
26 snow wetness (Tedesco, 2015; Leinss et al., 2014). In addition, the operating cost  
27 of LiDAR is sufficiently high and is also weather dependent (Deems et al., 2013).  
28 As a result, spaceborne SAR systems benefit from substantial coverage (globally  
29 available), cloud insensitivity, all-day operability and are extensively used to  
30 measure the snow physical properties sufficiently at high spatial resolutions  
31 (Moreira et al., 2013; Thakur et al., 2012).

32 The applicability of SAR systems for snow cover monitoring was discussed  
33 as early as 1977 (Ulaby et al., 1977) wherein the snow backscatter coefficient  
34 was measured and was thereafter modelled for various frequencies, layers, and  
35 polarisations (Zuniga et al., 1979). It was shown that only very high microwave  
36 frequencies (Ku-band or higher) exhibit a significant dependence on SD or  
37 the SWE of dry or standing (deposited) snow (Yueh et al., 2009). However,  
38 lower frequencies (X-band or below) penetrate through dry snow whereby the  
39 underneath frozen soil or ground primarily contributes to the radar backscatter  
40 signal. Whereas, in case of moist snow (the transitional stage between dry  
41 and wet snow) and wet snow, the predominant scattering occurs from the snow

42 volume and snow surface respectively due to the presence of water. Essentially,  
43 water, with its high dielectric constant, heavily modifies the dielectric properties  
44 of snow and effectively reduces the snow penetration capacity of the radar  
45 pulses ([Abe et al., 1990](#)). The radar backscattering mechanism for a typical  
46 snow covered area can be conceptualised from Figure 1.1. In principle, PolSAR  
47 and InSAR systems utilise these received target echoes for supporting various  
48 microwave remote sensing applications in the cryosphere domain.

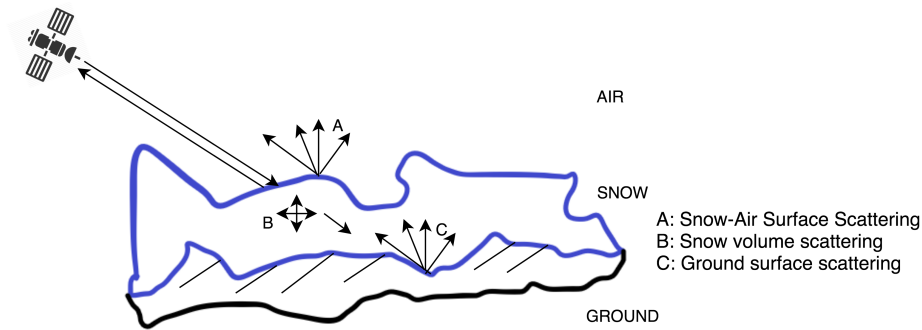


Figure 1.1: Conceptual diagram displaying the radar backscattering mechanism in hilly terrains. Adapted from [Thakur et al. \(2012\)](#).

49 PolSAR based algorithms which work on the polarimetric backscatter signal  
50 have been widely adopted for various snow related applications such as the  
51 classification of dry and wet snow, measuring snow wetness and snow density  
52 ([Singh et al., 2017](#); [Snehmani et al., 2010](#); [Thakur et al., 2012, 2017](#); [Usami  
53 et al., 2016](#)). [Leinss et al. \(2014\)](#) introduced the use of spaceborne PolSAR for  
54 snow height determination, wherein the relationship between the copolar phase  
55 difference (CPD) and fresh snow depth (FSD) is quantitatively analysed by  
56 deriving a theoretical model ([Leinss et al., 2014](#)). Moreover, InSAR techniques  
57 find significant usage in the cryosphere domain and have been used to measure  
58 dry snow depth and SWE in several studies ([Conde et al., 2019](#); [Gneriussen  
59 et al., 2001](#); [Leinss et al., 2015](#); [Li et al., 2017](#); [Liu et al., 2017](#)). In this  
60 context, the Pol-InSAR technique works on the coherent combination of both  
61 PolSAR and InSAR observations, thereby enabling the interferogram generation

62 in arbitrary transmit and receive channels (Papathanassiou & Cloude, 2001;  
63 Cloude, 2005, 2010). It has been widely used for estimating tree height in  
64 forested regions and can be effectively applied to natural or artificial volume  
65 scatterers including snow and ice (Leinss et al., 2014; Hajnsek et al., 2009;  
66 Kugler et al., 2015; Kumar et al., 2017; Papathanassiou & Cloude, 2001).

67 The prime focus of this research is to estimate the FSD and SSD using  
68 PolSAR and Pol-InSAR respectively. Additionally, the corresponding fresh  
69 SWE (FSWE) and standing SWE (SSWE) are to be determined, for which  
70 the respective snow densities need to be known. In this work, the PolSAR  
71 CPD method (Leinss et al., 2014) is reproduced which shows high FSD and  
72 FSWE accuracies of 94.83% and 94.84% respectively. The main innovation  
73 lies in improving the Pol-InSAR based hybrid DEM differencing and coherence  
74 amplitude inversion model (Cloude, 2005, 2010). The SSD and SSWE results  
75 are estimated with accuracies of 99.53% and 99.48% respectively. These  
76 results are obtained after performing thorough sensitivity analysis of the free  
77 model parameters. Furthermore, the scattering characteristics of the study  
78 area are analysed using the dual-pol entropy ( $H$ ) and scattering angle ( $\alpha$ ) or  
79  $H/\alpha$  decomposition, and unsupervised Wishart classification techniques (Lee  
80 & Pottier, 2009; Cloude, 2010; Singh et al., 2014) for identifying the potential  
81 uncertainty sources.

82 This manuscript is compartmentalised into five sections each consisting  
83 of several subsections. It starts with an introductory discussion in section  
84 1. Thereafter, the methods involved in this work are described in section 2  
85 following which the study area and the datasets including the required software  
86 are specified in section 3. The results are discussed in section 4. Finally, the  
87 relevant conclusions and recommendations are put forward in section 5.

## 88 2. Methodology

89 This section deals with the methodological framework which has been  
90 followed to generate the SD and SWE results. In order to briefly put the

91 overall workflow, a flowchart is shown in Figure 2.1 which highlights the main  
 92 process blocks. Here, the preprocessing steps are discussed in section 2.1.  
 93 Moreover, the PolSAR CPD and Pol-InSAR based approaches used for the  
 94 FSD and SSD estimation respectively are individually addressed in sections 2.2  
 95 and 2.3. Finally, the uncertainty assessment, validation and sensitivity tasks  
 96 are described in section 2.4.

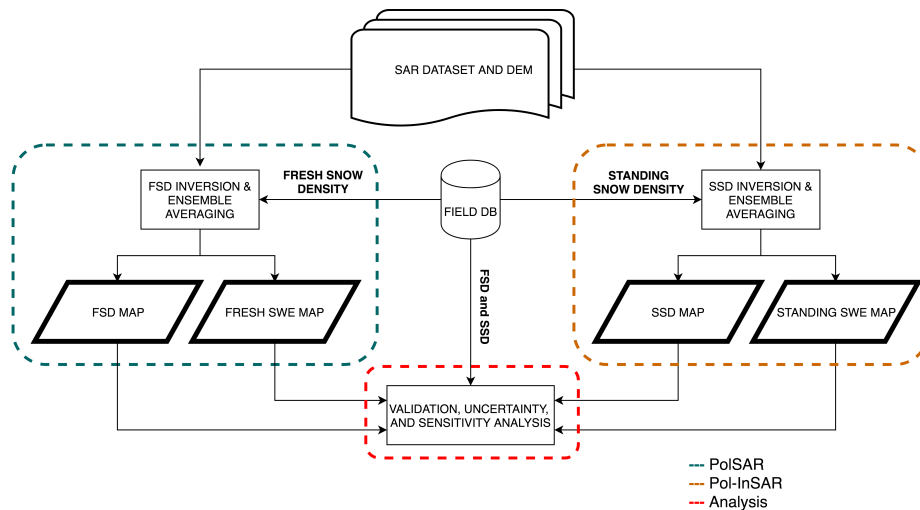


Figure 2.1: Overview of the main processing blocks.

97 *2.1. Data Preprocessing*

98 Since the SAR dataset is already coregistered, separate coregistration step  
 99 has not been performed. In case of the FSD estimation model, the geocoded or  
 100 terrain-corrected data (3 m spatial resolution) consists of the HH and VV scenes  
 101 along with the local incidence angle (LIA) computed from the ALOS PALSAR  
 102 DEM. As for the Pol-InSAR scenario, all the SAR channels, i.e., HH, HV, VH  
 103 and VV along with the LIA are present in the geocoded data. It should be  
 104 noted that, for the Pol-InSAR, processing both the master, TDX (master) and  
 105 TSX (slave) images are required to generate the interferogram. However, the  
 106 FSD estimation model can be used using any one of these images, though the

107 average of the TDX and TSX CPDs can potentially improve the signal-to-noise  
108 ratio (SNR) (Leinss et al., 2014).

## 109 2.2. CPD based Fresh Snow Depth Estimation

### 110 2.2.1. CPD Computation

111 The FSD is estimated using the CPD method developed by Leinss et al.  
112 (2014). At first,  $\phi_{CPD}$  for the TDX data ( $\phi_{CPD,TDX}$ ) acquired on January 8,  
113 2016, is computed using Eq. (2.1a) and then an ensemble averaging operation is  
114 applied over a  $21 \times 21$  window (Majumdar et al., 2019). Similarly,  $\phi_{CPD}$  for the  
115 TSX data ( $\phi_{CPD,TSX}$ ) is calculated following which the average CPD,  $\overline{\phi_{CPD}}$  is  
116 obtained using Eq. (2.1b). Here,  $\Im$  and  $\Re$  denote the imaginary and real parts  
117 of the complex scattering matrices  $S_{VV}$  and  $S_{HH}$  respectively.

$$\phi_{CPD} = \phi_{VV} - \phi_{HH} = \left\langle \underbrace{\tan^{-1} \left( \frac{\Im(S_{VV})}{\Re(S_{VV})} \right)}_{\phi_{VV}} - \underbrace{\tan^{-1} \left( \frac{\Im(S_{HH})}{\Re(S_{HH})} \right)}_{\phi_{HH}} \right\rangle \quad (2.1a)$$

$$\overline{\phi_{CPD}} = \frac{\phi_{CPD,TDX} + \phi_{CPD,TSX}}{2} \quad (2.1b)$$

118  $\phi_{CPD}$  can be alternatively defined as the phase angle of the complex copolar  
119 coherence,  $\tilde{\gamma}_c$  (since  $\gamma$  is the standard notation for coherence amplitude,  $\tilde{\gamma}$   
120 is used for the complex coherence), defined in Eq. (2.2). In this case, the  
121 copolar coherence amplitude ( $\gamma_c = |\tilde{\gamma}_c|$ ) is a measure of the radar backscattering  
122 mechanism where low values close to zero (ideally  $\gamma_c = 0$ ) indicate the presence  
123 of volume scattering and high values (ideally  $\gamma_c = 1$ ) represent surface scattering  
124 (Lee & Pottier, 2009; Leinss et al., 2014; Singh et al., 2014). It should be noted  
125 that only the CPD computed from side-looking radar systems is able to describe  
126 a target having dielectrically anisotropic microstructure as in the case of snow  
127 (Leinss et al., 2014).

$$\tilde{\gamma}_c = \frac{\langle S_{VV} S_{HH}^* \rangle}{\sqrt{\langle S_{VV} S_{VV}^* \rangle \langle S_{HH} S_{HH}^* \rangle}} = \gamma_c e^{j\phi_{CPD}}, \gamma_c \in [0, 1] \quad (2.2)$$

128 where,  $j$  is the imaginary unit.

129 *2.2.2. Depolarisation Factor Estimation*

130 In order to model this snow anisotropy, an ice particle needs to be associated  
 131 with a specific shape. It has been observed that fresh snow and old snow  
 132 exhibit horizontally aligned (oblate) and vertically aligned (prolate) spheroidal  
 133 structures respectively (Leinss et al., 2014). Moreover, a shape parameter,  
 134 known as the depolarisation factor, also has to be considered in this context  
 135 (Leinss et al., 2014; Sihvola, 1999). In principle, a single spheroidal particle is  
 136 characterised by three dipoles corresponding to the three orthogonal axes ( $a_x$ ,  
 137  $a_y$ , and  $a_z$ ) represented using a 3D ( $x, y, z$ ) Cartesian coordinate system. This is  
 138 depicted in Figure 2.2, where the prolate shaped ice grain is linked with the radar  
 139 reference frame ( $h, k, v$ ) following the radar backscattering alignment (BSA)  
 140 convention,  $k$  being the propagation vector,  $h$  and  $v$  are the wave components  
 141 of the horizontal and vertical polarisations respectively. Also,  $\theta$  is the mean  
 142 incidence angle with respect to the surface normal (Leinss et al., 2014; Parrella  
 143 et al., 2013).

144 Therefore, by fixing a particle shape, the three depolarisation factors,  $N_i$   
 145 ( $\forall i \in \{x, y, z\}$ ), can be obtained by solving the surface integral ( $s$  is the  
 146 ellipsoidal surface) as shown in Eq. (2.3).

$$N_i = \frac{a_x a_y a_z}{2} \int_0^\infty \frac{ds}{(s + a_i^2) \sqrt{(s + a_x^2)(s + a_y^2)(s + a_z^2)}} \quad (2.3)$$

147 where,  $N_x + N_y + N_z = 1$ .

148 For a perfectly spherical shape, all three depolarisation factors are equal to  
 149 1/3. The two other special cases include disk (1, 0, 0) and needle (0, 1/2, 1/2).  
 150 In cases of prolate and oblate spheroids, the closed form expressions are already  
 151 available as shown in Eq. (2.4) (Sihvola, 1999). Here, the shape is dependent  
 152 on the axial ratio ( $a_x/a_z$ ) which is used for calculating the prolate eccentricity,  
 153  $e_1 = \sqrt{1 - (a_x/a_z)^2}$ , and oblate eccentricity,  $e_2 = \sqrt{(a_x/a_z)^2 - 1}$  respectively,  
 154 i.e., for prolate,  $a_x/a_z < 1$ , whereas for oblate, it is the reverse. However, for  
 155 general ellipsoids having different axes, the above surface integration needs to  
 156 be explicitly solved.



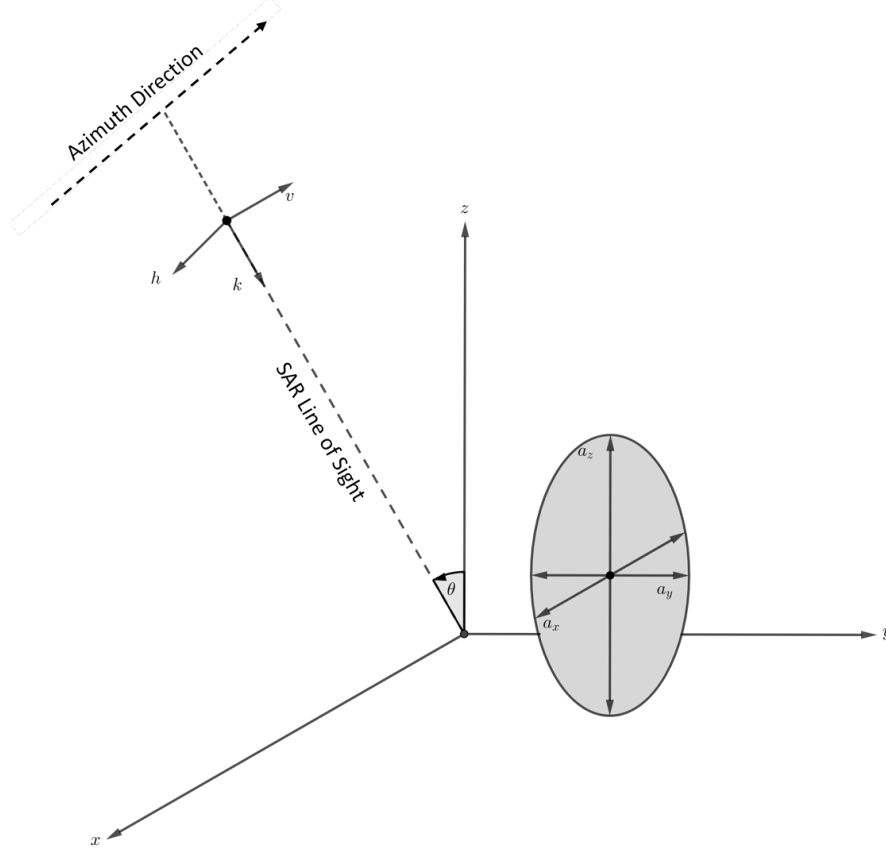


Figure 2.2: Orientation of a single prolate ice particle linked with the radar reference frame. Adapted from [Leinss et al. \(2014\)](#).

$$N_z = \begin{cases} \frac{1-e_1^2}{2e_1^3} \left( \ln \frac{1+e_1}{1-e_1} - 2e_1 \right) & , a_z > a_x = a_y \\ \frac{1+e_2^2}{e_2^3} \left( e_2 - \tan^{-1} e_2 \right) & , a_z < a_x = a_y \end{cases} \quad (2.4)$$

157 *2.2.3. Snow Refractive Index Estimation*

158 Evidently, the Maxwell-Garnett theory related to electromagnetic mixing  
 159 models can be applied to a medium (here snow) consisting of both air and ice  
 160 which are having relative permittivities (real part),  $\epsilon_{air}$  and  $\epsilon_{ice}$  respectively.  
 161 Therefore, the effective permittivity of this mixed medium,  $\epsilon_{eff,i}$ , is anisotropic  
 162 and given by Eq. (2.5) ([Leinss et al., 2014](#); [Sihvola, 1999](#)). Here, the particle

163 volume fraction ( $f_{vol}$ ) is dependent on the fresh snow density ( $\rho_f$ ) and ice density  
164 ( $\rho_{ice}$ ).

$$\epsilon_{eff,i} = \epsilon_{air} \left[ 1 + f_{vol} \frac{\epsilon_{ice} - \epsilon_{air}}{\epsilon_{air} + (1 - f_{vol}) N_i (\epsilon_{ice} - \epsilon_{air})} \right] \quad (2.5)$$

165 where,  $f_{vol} = \rho_f / \rho_{ice}$ ,  $\rho_{ice} = 0.917 \text{ g/cm}^3$ ,  $\epsilon_{air} = 1.00059$ ,  $\epsilon_{ice} = 3.179$ , and  $i \in$   
166  $\{x, y, z\}$ .

167 Furthermore, the refractive indices of this birefringent (or birefractive)  
168 medium,  $n_H$  and  $n_V$  corresponding to the HH and VV polarisations respectively,  
169 are dependent on this anisotropic effective permittivity (Leinss et al., 2014).  
170 In addition, since the snow anisotropy is assumed to be oriented along the  
171 Earths gravitational field,  $n_H$  remains constant whereas  $n_V$  is dependent on the  
172 incidence angle  $\theta$  as given by Eq. (2.6a) and Eq. (2.6b) respectively (Leinss  
173 et al., 2016). Also, the imaginary part of the effective permittivity is negligible  
174 in the case of dry snow (fresh snow is also dry), and therefore, it is not used in  
175 the model developed by Leinss et al. (2014).

$$n_H^2 = \epsilon_{eff,x} \quad (2.6a)$$

$$n_V^2 = \epsilon_{eff,y} \cos^2 \theta + \epsilon_{eff,z} \sin^2 \theta \quad (2.6b)$$

176 where,  $\epsilon_{eff,x}$ ,  $\epsilon_{eff,y}$ , and  $\epsilon_{eff,z}$  represent the effective permittivities of fresh  
177 snow in  $x$ ,  $y$ , and  $z$  directions of a 3D Cartesian co-ordinate system (Leinss  
178 et al., 2014).

#### 179 2.2.4. FSD and FSWE Computation

180 Once all these aforementioned parameters are calculated, the CPD based  
181 inversion model given by Eq. (2.7) is applied to estimate the depth of fresh  
182 snow, denoted by  $\Delta Z_f$  (Majumdar et al., 2019; Leinss et al., 2014, 2016). In  
183 this equation, -1 is introduced as per the BSA convention which is followed for  
184 all radar systems. Here,  $\lambda_0$  is the radar wavelength and  $\Delta \zeta$  is the relative path  
185 length difference which is dependent on  $\epsilon_{eff,i}$ ,  $\theta$ , and  $\rho_f$  (Leinss et al., 2016).  
186 Moreover, the horizontally aligned microstructure of fresh snow reduces the

187 propagation speed for the HH channel and hence, in this case,  $n_H > n_V$  always  
 188 holds. However, for recrystallised snow having vertically aligned structures, the  
 189 reverse condition is true (Leinss et al., 2016). Also, the LIA ( $\theta_l$ ) is used instead  
 190 of the mean incidence angle ( $\theta$ ) to consider the effect of the terrain slope.

$$\Delta Z_f = \left\langle (-1) \frac{\lambda_0 \phi_{CPD}}{4\pi \Delta \zeta} \right\rangle \quad (2.7)$$

191 where,  $\Delta \zeta = \sqrt{n_V^2 - \sin^2 \theta_l} - \sqrt{n_H^2 - \sin^2 \theta_l}$ ,  $\phi_{CPD} > 0$ , and  $n_H > n_V$ .

192 Here, the depolarisation factors are calculated by setting the axial ratio,  
 193  $a_x/a_z = 1.5$  in Eq. (2.4) and choosing the snow particle shape as an oblate  
 194 (Majumdar et al., 2019). After this, the anisotropic effective permittivities  
 195 are computed using Eq. (2.5). Finally, the FSD is obtained from Eq. (2.7)  
 196 wherein an ensemble averaging filter of size  $65 \times 65$  is applied. The FSWE is  
 197 obtained by multiplying the FSD with the fresh snow density (i.e, FSWE =  
 198  $\rho_f \Delta Z_f$ ). Also, the fresh snow density ( $\rho_f = 0.07 \text{ g/cm}^3$ ) which is manually  
 199 measured at Dhundi, is kept constant for the entire study area along with the  
 200 copolar coherence threshold,  $\tau_c = 0$  ( $\tau_c \in [0, 1]$ ), i.e., no thresholding has been  
 201 applied on  $\gamma_c$  computed using Eq. (2.2), but the provision for it is built-in  
 202 to the implementation. Moreover, as per the TSX/TDX metadata, the radar  
 203 wavelength,  $\lambda_0 \approx 3.11 \text{ cm}$ . In this context, the adopted workflow is depicted in  
 204 Figure 2.3.

### 205 *2.3. Pol-InSAR based Standing Snow Depth Estimation*

206 Standing or old snow refers to the deposited snow on the ground which has  
 207 accumulated over time (Reynolds, 1983). Typically, old snow due to the presence  
 208 of impurity and temperature-gradient induced recrystallisation process consists  
 209 of snow particles larger than the microwave wavelength and results in volume  
 210 scattering (Leinss et al., 2016; Riche et al., 2013). This volume decorrelation can  
 211 be quantitatively analysed with the help of the Pol-InSAR technique (Cloude,  
 212 2010) to obtain the volumetric SSD ( $\Delta Z_s$ ).

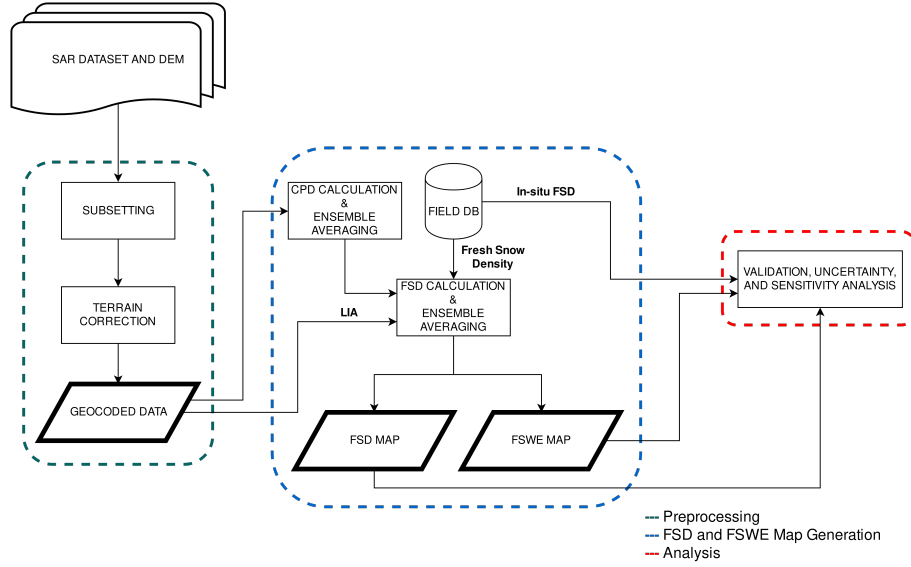


Figure 2.3: FSD and FSWE estimation workflow using PolSAR CPD. This workflow represents a detailed overview of the FSD and FSWE processing block in Figure 2.1.

### 2.3.1. Single-baseline Pol-InSAR Specifics

213 The single baseline Pol-InSAR algorithm works on the basis of the complex  
 214 coherence,  $\tilde{\gamma}(\vec{w}_1, \vec{w}_2)$ , defined in Eq. (2.8a) where  $I_i(\vec{w}_1, \vec{w}_2)$  denotes the  $i^{\text{th}}$   
 215 pixel coordinate value of the wrapped Pol-InSAR interferogram,  $I(\vec{w}_1, \vec{w}_2)$   
 216 obtained in Eq. (2.8b). This interferogram is calculated from Eq. (2.8c) and Eq.  
 217 (2.8d) where the coregistered master ( $s_1$ ) and slave ( $s_2$ ) images are acquired at  
 218 a given polarisation vector,  $(\vec{w})$  respectively. Here, the weight vectors,  $\vec{w}_1$  and  
 219  $\vec{w}_2$  are selected by the user based on the scattering mechanisms at ends 1 and  
 220 2 of the interferometric baseline. If  $\vec{w}_1 = \vec{w}_2$ ,  $\tilde{\gamma}(\vec{w}_1, \vec{w}_2)$  can be alternatively  
 221 specified as  $\tilde{\gamma}(\vec{w}_1)$  (Cloude, 2005, 2010). Moreover,  $L$  is the total number of  
 222 pixels averaged in the range and azimuth directions which can be replaced by  
 223 the ensemble averaging operation following the statistical ergodicity assumption  
 224 (Hanssen, 2001; Hoen & Zebker, 2000; Kugler et al., 2015; Kumar et al., 2017;  
 225 Papathanassiou & Cloude, 2001). Additionally,  $\phi_{flat}^w \in [0, 2\pi)$  is the wrapped  
 226 flat-earth phase obtained from the estimated absolute flat-earth phase,  $\phi_{flat}$  and  
 227

228 has to be removed from  $I(\vec{w}_1, \vec{w}_2)$  as shown in Eq. (2.8b). Also, the calculation  
 229 of the generalised weight vector,  $\vec{w}$  is given by Eq. (2.8e).

$$\tilde{\gamma}(\vec{w}_1, \vec{w}_2) = \frac{\sum_{i=1}^L I_i(\vec{w}_1, \vec{w}_2)}{\sqrt{\sum_{i=1}^L |s_{1i}(\vec{w}_1)|^2 \sum_{i=1}^L |s_{2i}(\vec{w}_2)|^2}}, |\tilde{\gamma}(\vec{w}_1, \vec{w}_2)| \in [0, 1] \quad (2.8a)$$

$$I(\vec{w}_1, \vec{w}_2) = s_1(\vec{w}_2) s_2^*(\vec{w}_2) e^{-j\phi_{flat}} \quad (2.8b)$$

$$s_1 = w_1^1 \frac{s_{hh}^1 + s_{vv}^1}{\sqrt{2}} + w_1^2 \frac{s_{hh}^1 - s_{vv}^1}{\sqrt{2}} + w_1^3 \sqrt{2} s_{hv}^1 \quad (2.8c)$$

$$s_2 = w_2^1 \frac{s_{hh}^2 + s_{vv}^2}{\sqrt{2}} + w_2^2 \frac{s_{hh}^2 - s_{vv}^2}{\sqrt{2}} + w_2^3 \sqrt{2} s_{hv}^2 \quad (2.8d)$$

$$\vec{w} = \begin{bmatrix} w^1 & w^2 & w^3 \end{bmatrix}^T = \begin{bmatrix} \cos \alpha & \sin \alpha \cos \beta e^{j\delta} & \sin \alpha \sin \beta e^{j\mu} \end{bmatrix}^T \quad (2.8e)$$

230 where,  $s_{pp}^1$  and  $s_{pp}^2$  correspond to the master (1) and slave (2) images  
 231 respectively,  $pp \in \{hh, hv, vv\}$ , and  $*$  denotes the complex conjugate operator.

232 In this case, the parameters, scattering alpha angle ( $\alpha$ ), target orientation  
 233 angle ( $\beta$ ), phase terms ( $\delta$  and  $\mu$ ), are chosen according to the selected  
 234 polarisation given by Table 2.1. Here, LL, LR and RR correspond to the  
 235 left circular, left-right circular and right circular polarisations (Cloude, 2010).  
 236 However, it is possible to optimise these parameters specific to the data, the  
 237 details of which are provided by Cloude (2010).

Table 2.1: Pol-InSAR scattering mechanisms (Cloude, 2005).

Polarisation Selection	$\alpha(^{\circ})$	$\beta(^{\circ})$	$\delta(^{\circ})$	$\mu(^{\circ})$
HH	45	0	0	0
HV	90	90	0	0
VV	45	180	0	0
HH+VV	0	0	0	0
HH-VV	90	0	0	0
LL	90	45	0	90
LR	0	0	0	0
RR	90	45	0	-90

238 *2.3.2. Height Inversion Algorithm Details*

239 In this study, the modified (also improved) hybrid DEM differencing and  
240 coherence amplitude based Pol-InSAR volumetric height inversion model as  
241 given by Eq. (2.9a) is used for the SSD estimation. Firstly, the volume scattering  
242 dominant channels, HV and VH, are averaged to fully utilise the quad-pol data  
243 (Cloude, 2005). Next, the Pol-InSAR interferogram,  $I(\vec{w}_v)$  has been computed  
244 using Eq. (2.8b) wherein, the weight vector,  $\vec{w}_v$  is obtained from Table 2.1  
245 for the HV polarisation. Thereafter, the complex volume coherence,  $\tilde{\gamma}(\vec{w}_v)$ ,  
246 is calculated from Eq. (2.8a) with  $L = 3$ . Similarly, the complex surface or  
247 ground coherence,  $\tilde{\gamma}(\vec{w}_s)$ , is computed by choosing  $\vec{w}_s$  as the HH-VV weight  
248 vector (Table 2.1).

249 Moreover, the actual vertical wavenumber,  $k_z$ , when varied with the LIA, is  
250 in the order of 0.1 rad/m with the ambiguity height,  $h_{2\pi} = 2\pi/k_z \approx 63.18$  m,  
251  $\lambda_0 \approx 3.11$  cm and  $m = 1$  (single-pass acquisition). Since the maximum height of  
252 the distributed volume scatterer (in this case, standing snow),  $\Delta Z_{s,max}$ , should  
253 be similar to  $h_{2\pi}$  (Kugler et al., 2015; Hajnsek et al., 2009; Kumar et al., 2017),  
254  $k_z$  has to be rescaled to an optimum range for effectively estimating the SSD.  
255 Hence, the modified vertical wavenumber,  $k'_z$ , is given by Eq. (2.9b) where  $\eta'$   
256 is a free scaling parameter which has to be set according to the known  $\Delta Z_{s,max}$   
257 in the study area. Here,  $h'_{2\pi}$  is the scaled height of ambiguity which like that  
258 of  $h_{2\pi}$  determines the height changes in modulo  $2\pi$  (Hanssen, 2001). Also,  $\mathbb{R}^+_{>0}$   
259 denotes the set of all positive real numbers in the interval  $(0, \infty)$ . In this work,  
260 due to the limited ground-truth data availability and the subsequent ensemble  
261 averaging operation (window size of  $21 \times 21$ ) on  $k'_z$ ,  $\Delta Z_{s,max} = 12$  m has been  
262 assumed for which  $\eta' = 5$  is used.

263 Apart from this, the function  $\arg$  is defined in the interval  $[0, 2\pi)$  and the  
264 parameter  $m$  is set to 1 for bistatic acquisition and 2 in the monostatic case.  
265 Also in Eq. (2.9b),  $\Delta\theta$  is the change in the incidence angle occurring due to  
266 the spatial baseline,  $\theta_l$  is the LIA, and  $\lambda_0$  is the radar wavelength as before in

267 section 2.2 (Cloude, 2010; Kugler et al., 2015).

$$\Delta Z_s = \frac{\arg\left(\tilde{\gamma}(\vec{w}_v) e^{-j\phi_{topo}^w}\right)}{k'_z} + \eta \frac{\text{sinc}_\pi^{-1}(\gamma(\vec{w}_v))}{k'_z}, \eta \in [0, 1] \quad (2.9a)$$

268 where,

$$k'_z = \left\langle \eta' \frac{m\Delta\theta}{\lambda_0 \sin\theta_t} \right\rangle, \eta' \in \mathbb{R}_{>0}^+ \mid \Delta Z_{s,max} \approx h'_{2\pi} = 2\pi/k'_z \quad (2.9b)$$

269 Subsequently, the volume and surface coherences are then used to estimate  
 270 the wrapped ground phase,  $\phi_{topo}^w \in [0, 2\pi)$ , from Eq. (2.10). Additionally, a  
 271 median ensemble filter of  $21 \times 21$  is applied on the obtained  $\phi_{topo}^w$  following the  
 272 processing steps provided by Cloude (2005).

$$\phi_{topo}^w = \arg\left(\tilde{\gamma}(\vec{w}_v) - \tilde{\gamma}(\vec{w}_s)(1 - L_{\vec{w}_s})\right) \quad (2.10)$$

where,

$$L_{\vec{w}_s} = \frac{-B - \sqrt{B^2 - 4AC}}{2A}, L_{\vec{w}_s} \in [0, 1]$$

$$A = |\tilde{\gamma}(\vec{w}_v)|^2 - 1$$

$$B = 2\Re(\tilde{\gamma}(\vec{w}_v) - \tilde{\gamma}(\vec{w}_s)\tilde{\gamma}^*(\vec{w}_v))$$

$$C = |\tilde{\gamma}(\vec{w}_v) - \tilde{\gamma}(\vec{w}_s)|^2$$

273 Eventually, the SSD ( $\Delta Z_s$ ) and SSWE ( $= \rho_s \Delta Z_s$ ) are estimated wherein  
 274 the standing snow density ( $\rho_s = 0.315 \text{ g/cm}^3$ ) measured by the Dhundi SPA at  
 275 06:22 hrs IST on January 8, 2016, has been used. Here,  $\eta = 0.65$ , the volume  
 276 coherence threshold,  $\tau_v = 0.6$  (pixels having  $\tau_v < 0.6$  are neglected  $\forall \tau_v \in [0,$   
 277  $1]$ ), and the SSD values are averaged based on a  $57 \times 57$  ensemble filter window.  
 278 The entire Pol-InSAR workflow is summarised in Figure 2.4 which shows the  
 279 main processing blocks.

280 However, in order to compute the inverse  $\text{sinc}_\pi$  (normalised sinc) function  
 281 in Eq. (2.9a), the Cloude (2010) approximation ( $\text{sinc}_C^{-1}$ ) in Eq. (2.11a) is  
 282 replaced by Eq. (2.11b) where the secant method (Cheney & Kincaid, 2012)  
 283 has been applied to find  $\alpha_r \in \mathbb{R}$  (rad), the desired root or inverse. Moreover, to

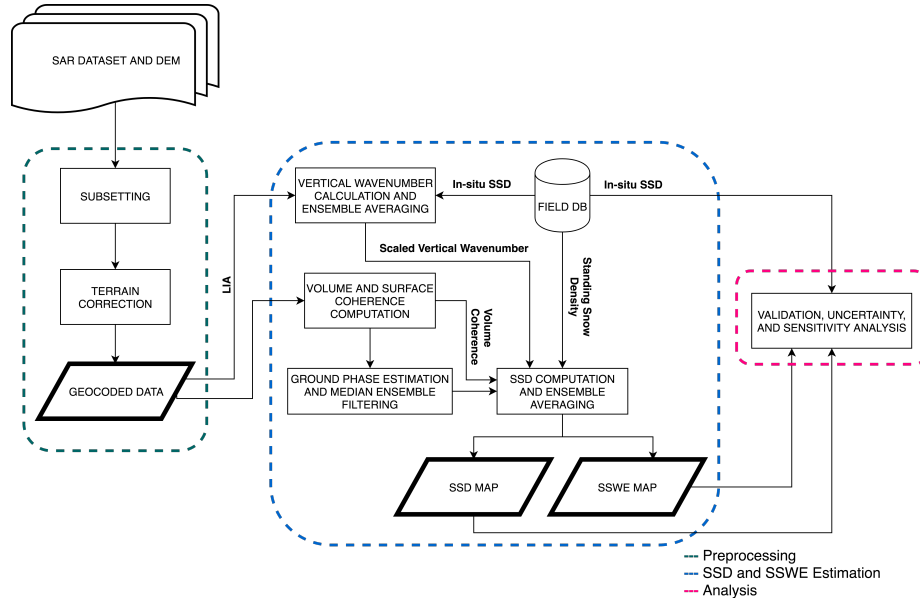


Figure 2.4: SSD and SSWE estimation workflow using Pol-InSAR depicting a detailed overview of the SSD and SSWE processing block in Figure 2.1.

284 make the [Cloude \(2010\)](#) approximation compliant with the scientific computing  
 285 libraries such as SciPy ([Jones et al., 2001](#)) which use the  $\text{sinc}_\pi$  function, the  
 286 normalised variant of Eq. (2.11a) given by Eq. (2.11c) is incorporated where  
 287  $\text{sinc}_{\pi_C}^{-1}$  denotes the inverse of the  $\text{sinc}_\pi$  function computed using the [Cloude](#)  
 288 (2010) approach. Similarly,  $\text{sinc}_{\pi_S}^{-1}$  represents the inverse of the  $\text{sinc}_\pi$  function  
 289 obtained by applying the secant method ([Cheney & Kincaid, 2012; Jones et al.,](#)  
 290 [2001](#)). This root finding technique has been deployed as it is more accurate  
 291 than the given approximation in Eq. (2.11c), the analysis of which is described  
 292 in section 4. Still, in the Python implementation, this approximation is used as  
 293 an initial guess to the secant method for faster convergence. It is also used as a  
 294 fallback option if the secant method is unable to converge within 50 iterations



295 or the default convergence threshold of 1.4E-8 (Jones et al., 2001).

$$\text{sinc}_C^{-1}(\gamma(\vec{w}_v)) = \pi - 2 \sin^{-1}\left(\gamma(\vec{w}_v)^{0.8}\right) \quad (2.11a)$$

$$\text{sinc}_\pi \alpha_r - \gamma(\vec{w}_v) = 0 \quad (2.11b)$$

$$\text{sinc}_{\pi_C}^{-1}(\gamma(\vec{w}_v)) = \frac{\text{sinc}_C^{-1}(\gamma(\vec{w}_v))}{\pi} \quad (2.11c)$$

## 296 2.4. Validation, Uncertainty Assessment, and Sensitivity Analysis

### 297 2.4.1. Validation Process

298 One of the significant challenges in this work is the limited ground-truth  
 299 data availability. Since, in-situ data from only two ground stations are available,  
 300 the conventional way of accuracy assessment through regression plots (Kugler  
 301 et al., 2015; Leinss et al., 2014; Kumar et al., 2017) is infeasible in this context.  
 302 Moreover, the Kothi AWS area falls in the layover region for the descending  
 303 pass acquisitions and hence, only the Dhundi region which is free from layover,  
 304 shadow and foreshortening effects, is used for validation. In this case, a  
 305 neighbourhood window of size 3×3 ( $\approx 81 \text{ m}^2$  ground area) surrounding the  
 306 Dhundi SPA is selected for validating the SD and SWE estimates by considering  
 307 only the statistical mean and standard deviation.

### 308 2.4.2. Uncertainty Assessment

309 Due to the complex terrain characteristics there exist significant uncertainty  
 310 sources which could potentially lead to the overall degradation of the output  
 311 accuracy. Having the quad-pol data in winter time (January 8, 2016) and dual-  
 312 pol data in summer time, we are able to use dual-pol entropy ( $H \in [0, 1]$ ) and the  
 313 scattering alpha angle ( $\alpha \in [0^\circ, 90^\circ]$ ) or  $H/\alpha$  decomposition to comparatively  
 314 understand the backscattering mechanisms in these two time intervals (Cloude,  
 315 2010; Lee & Pottier, 2009; Singh et al., 2014). The 5×5 window size for the  $H/\alpha$   
 316 decomposition is used. This is carried out through the  $H/\alpha$  plane plot which  
 317 demarcates eight feasible zones (Z9 being the unclassified pixels) based on the  
 318 different scattering classes as shown in Figure 2.5. Note that, this diagram which

319 follows the SNAP style (ESA, 2018), uses slightly different labels as compared  
 320 to the Lee & Pottier (2009)  $H/\alpha$  plane convention where the labels Z1, Z2, Z3  
 321 are denoted as Z7, Z8, Z9 and vice-versa respectively. However, the scattering  
 322 mechanisms are exactly the same in both these conventions. Here, the blue  
 323 curve acts as a boundary to the plane which essentially denotes the reliability  
 324 of the classification in high entropy conditions (Brunner, 2009).

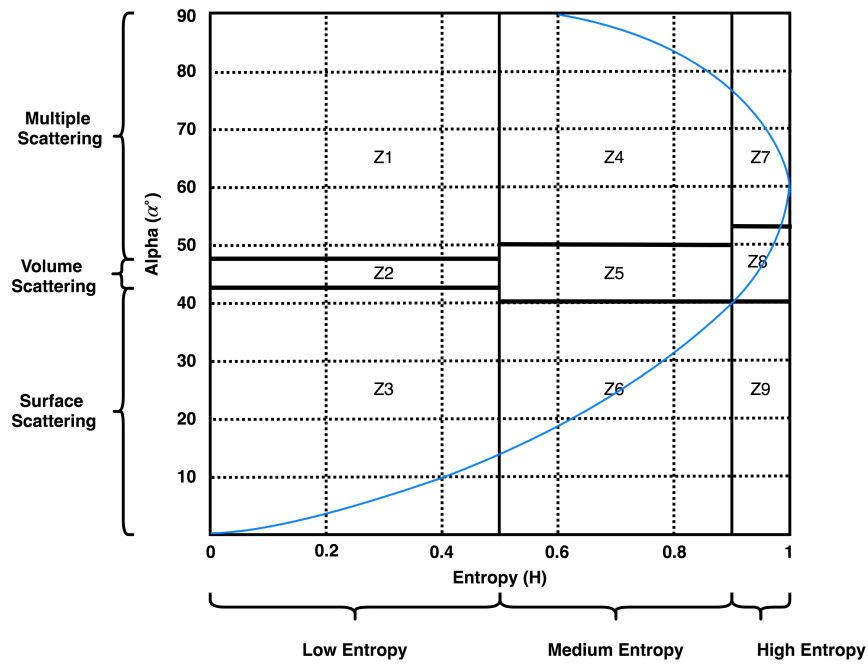


Figure 2.5:  $H/\alpha$  plane showing different scattering zones. Z1: Dihedral, Z2: Dipole, Z3: Bragg Surface, Z4: Double bounce, Z5: Anisotropic, Z6: Random surface, Z7: Complex structures, Z8: Random anisotropic, Z9: Non-feasible.

325 The dual-pol  $H/\alpha$  decomposition is further used by the unsupervised  
 326 Wishart classifier (ten iterations) which classifies the SAR data based on these  
 327 scattering mechanisms and a quantitative estimate of the number of pixels in  
 328 each such class can be obtained (Cloude, 2010; Lee & Pottier, 2009). Therefore,  
 329 by knowing the scattering properties, the terrain features present in the study  
 330 area can be understood along with their changes during the snow season. In  
 331 turn, these ground features which include rough surfaces, shrubs, boulders,

332 and human settlements reduce the copolar coherence amplitude ( $\gamma_c$ ) thereby  
333 leading to underestimated FSD results (Leinss et al., 2014, 2016). In addition,  
334 the decrease in the Pol-InSAR surface coherence amplitude, ( $\gamma(\vec{w}_v) = |\tilde{\gamma}(\vec{w}_v)|$ )  
335 may result in overestimated volumetric height (Cloude, 2010; Hajnsek et al.,  
336 2009; Kugler et al., 2015), in this case, SSD. Thus, the uncertainty assessment  
337 by means of the identification of the backscattering mechanisms constitutes a  
338 key role in this work.

339 Apart from this, the forest cover map (obtained from WRD, IIRS) along  
340 with the layover and shadow regions computed using SAR simulation are used  
341 to mask out the noisy pixels which degrade the quality of the results. This is a  
342 standard approach used in the studies focusing on snow property estimation in  
343 forested or alpine terrains (Leinss et al., 2014, 2016; Singh et al., 2017; Thakur  
344 et al., 2012; Usami et al., 2016).

#### 345 *2.4.3. Sensitivity Analysis*

346 The variation of the SD and SWE values corresponding to the changes  
347 in the free parameters in the FSD and SSD inversion models (window size,  
348 coherence threshold, scaling factors) are observed by iteratively running the  
349 algorithms and computing the statistical mean and standard deviation using the  
350 neighbourhood window discussed earlier in section 2.4.1. This helps in deciding  
351 the window shape and sizes and also choosing the optimum values for the several  
352 free parameters. Moreover, the accuracy of the root finding algorithm discussed  
353 in section 2.3 is also checked for some possible coherence values.

354 In addition, the ground elevation measurements acquired during the field  
355 visit to Dhundi and Kothi were compared with the ALOS PALSAR DEM  
356 elevations ( $z$ ). The effect of the DEM errors on the LIA,  $\theta_l$ , is then checked  
357 for performing the sensitivity analysis (SA) using Eq. (2.12) which incorporates  
358 the slope angles in  $x$  ( $\omega_x$ ) and  $y$  ( $\omega_y$ ) directions (pixel co-ordinate system where  
359  $z$  is the corresponding elevation value) derived from the DEM elevation values  
360 along with the radar incidence angle ( $\theta$ ) (Lee et al., 2000; Lee & Pottier, 2009).  
361 Here, the terms  $dz/dx$  and  $dz/dy$  refer to the rate of elevation ( $z$ ) change in

362 the  $x$  and  $y$  directions respectively.

$$\theta_l = \cos^{-1} \frac{\cos \omega_x \cos (\omega_y - \theta)}{\sqrt{\cos^2 \omega_y \sin^2 \omega_x + \cos^2 \omega_x}} \quad (2.12)$$

where,

$$\omega_x = \tan^{-1} \frac{dz}{dx}, \omega_y = \tan^{-1} \frac{dz}{dy}.$$

### 363 3. Study Area, Datasets, and Software

#### 364 3.1. Chosen Study Area

##### 365 3.1.1. Geographical Situation

366 The Beas river watershed near Manali, India is part of the north-western  
 367 Himalayas. Naturally, steep slopes and dense forests are prominent in this  
 368 region. The elevation typically varies from nearly 2500 m to more than 5000 m  
 369 in some places as observed in the reference ALOS PALSAR DEM (Figure 3.1).

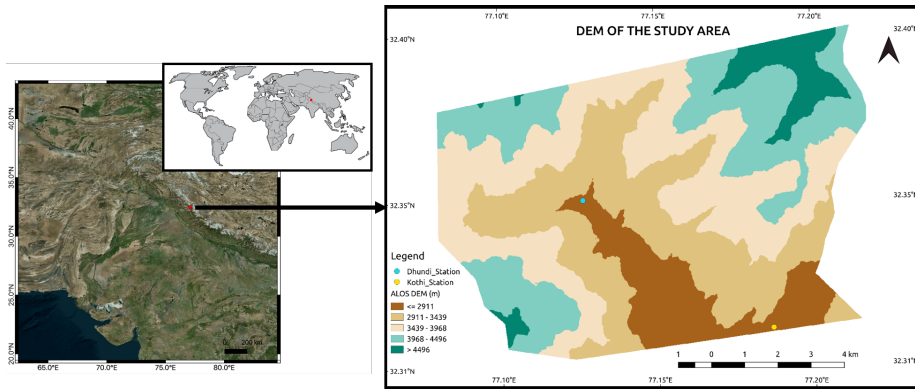


Figure 3.1: Overview map of the study area showing the ALOS PALSAR DEM. The original DEM of 12.5 m spatial resolution (generated in 2011) has been resampled to 3 m using bilinear interpolation (Wu et al., 2008) to match the high resolution SAR data. Moreover, the vertical resolution as per the product specification is 5 m.

370 In this work, a small region ( $\sim 96 \text{ km}^2$ ) of the Beas basin is chosen which  
 371 starts a few kilometres uphill from Dhundi up to Kothi (shown in Figure 3.1).  
 372 These areas receive substantial seasonal snowfall which begins in December and

373 lasts till late March. However, the cold, dry season usually commences from  
374 late September or early October. The coldest period is in January during which  
375 the temperatures reach a daily minimum of  $-15^{\circ}\text{C}$  on an average. The summers  
376 are mild to occasionally warm with June being the hottest month (mean and  
377 maximum temperatures of  $20^{\circ}\text{C}$  and  $30^{\circ}\text{C}$  respectively are common). Apart  
378 from this, significant rainfall occurs between late June and September (monsoon  
379 season) with August receiving the maximum precipitation ([Majumdar et al.,](#)  
380 [2019](#); [Thakur et al., 2012](#)).

### 381 *3.1.2. Field Visit*

382 Intensive fieldwork had been conducted from October 14-21, 2018 in the  
383 Dhundi and Kothi areas where several Differential Global Positioning System  
384 (DGPS) measurements were acquired using the Leica Viva GS 10 ([Leica](#)  
385 [Geosystems AG, 2012](#)) with adequate horizontal positional accuracies ( $\sim 7$  cm)  
386 ([Majumdar et al., 2019](#)). Due to the complex terrains, most of the DGPS  
387 readings had been obtained through the kinematic mode ([Luo et al., 2014](#)).  
388 However, in some of the convenient places such as the Dhundi base station and  
389 near the Kothi Automatic Weather Station (AWS), the static mode was used  
390 ([Leica Geosystems AG, 2012](#)). Eventually, elevation information from these  
391 DGPS points have been compared with the ALOS PALSAR DEM, the details  
392 of which are provided in section 4. Furthermore, the manual snow readings from  
393 2014-2018 (snow depth, density, weather profile and other relevant data) which  
394 are maintained by the security personnel daily at Dhundi had been pagewise  
395 photographed using a smartphone camera. In order to properly understand and  
396 visualise the characteristics of the study area, selected field photographs and  
397 their brief description are shown from figures [3.2\(a\)](#)-[3.2\(f\)](#).

### 398 *3.2. Datasets Used*

399 Overall twelve Coregistered Single look Slant range Complex (CoSSC)  
400 TerraSAR-X (TSX)/TanDEM-X (TDX) bistatic X-band SAR images acquired  
401 between December 2015 and August 2017 in stripmap (SM) mode are available



(a) DGPS positional accuracy checking



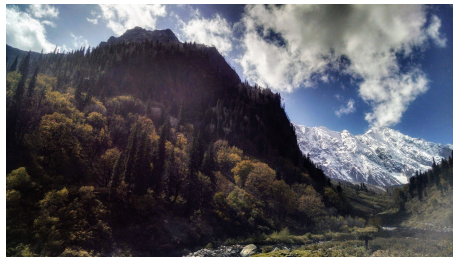
(b) Leica DGPS base



(c) Beas river



(d) Landscape and human settlements



(e) Mountains and forests



(f) Weather instruments

Figure 3.2: Dhundi field photographs showing the varying topographic features present in the surrounding area.

402 over this study area ([Balls et al., 2012](#)). In total, there are six Quad-pol data  
403 pairs, from which the descending orbital pass acquisition at 00:53 hrs Universal  
404 Time Coordinated (UTC), January 8, 2016, has been selected considering  
405 the occurrence of fresh snowfall before, during and after the satellite flyby.  
406 Moreover, the perpendicular baseline ( $B_{\perp}$ ) and ambiguity height ( $h_{2\pi}$ ) for this  
407 data are 96.34 m and 63.18 m respectively.

408 Additionally, the in-situ snow physical parameters data (standing and fresh  
409 snow depths, snow density) along with the relevant weather data had been

410 transferred to a PostgreSQL database (DB) ([PostgreSQL, 2019](#)) from the  
411 photographs of the manual recordings through spreadsheets. Apart from this,  
412 the high frequency data (two-minute interval measurements) obtained from the  
413 snowpack analyser (SPA) device (installed at Dhundi) had been downloaded and  
414 were added to the database as a separate table. Accordingly, the SSDs at 06:22  
415 hrs (00:52 hrs UTC) Indian Standard Time (IST) on January 7, 2016, and 06:22  
416 hrs January 8, 2016 morning were 36.2 cm and 54.9 cm respectively signifying  
417 a heavy fresh snowfall event of 18.7 cm within 24 hrs. The manual recordings  
418 also showed an FSD of 18 cm on January 8, 2016 morning though the exact  
419 measurement time is unspecified in the record book. Apart from this, a forest  
420 mask used in the earlier studies of this area ([Thakur et al., 2012, 2017](#)) has  
421 been obtained from the Water Resources Department (WRD), Indian Institute  
422 of Remote Sensing (IIRS).

423 The Sentinel Application Platform (SNAP) 6.0.5 ([ESA, 2018](#)) has been used  
424 for basic SAR processing. In addition, the FSD and SSD inversion models have  
425 been implemented using Python 3 wherein PyCharm Community Edition 2018.1  
426 ([JetBrains, 2018](#)) was used as the coding environment. Moreover, the final snow  
427 depth maps have been prepared using QGIS 2.18 ([QGIS, 2016](#)). Furthermore,  
428 some of the computationally intensive tasks have been carried out using the  
429 High-Performance Computing (HPC) infrastructure installed at IIRS.

## 430 **4. Results and Discussion**

### 431 *4.1. Scattering Mechanisms*

432 The winter (January 8, 2016) and summer-time (June 8, 2017) dual-pol  $H/\alpha$   
433 decomposition (Figure 4.3) and unsupervised Wishart classification (Figure 4.1)  
434 results combined with the derived class percentage statistics (Figure 4.2) show  
435 that, in the presence of snow, the high entropy anisotropic volume scattering  
436 (Z8) increases by 5.11% whereas the medium entropy volume scattering (Z5)  
437 decreases by 7.01% for the entire study area. This reduction in the Z5  
438 volume scattering could be attributed to the partially snow covered forests and

439 shrubs which exhibit higher volume scattering at X-band during the snow-free  
 440 season (Figure 3.2(e)). The corresponding dual-pol Wishart classified maps  
 441 are displayed along with the zoomed views in Figure 4.1(a) and Figure 4.1(b)  
 442 respectively.

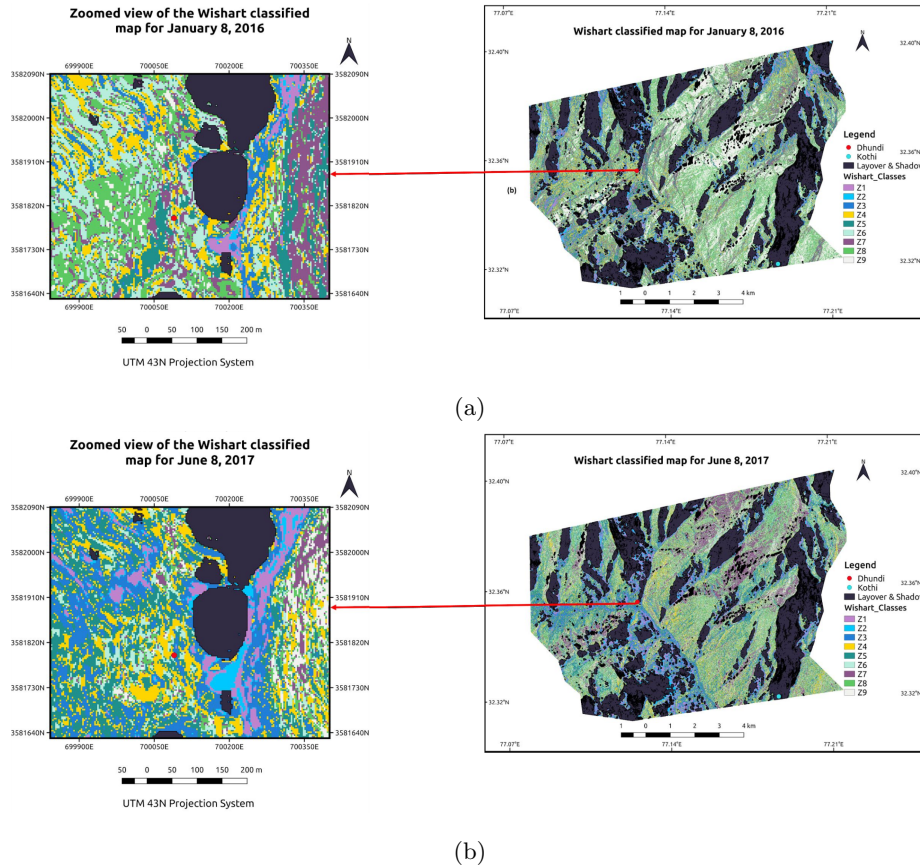


Figure 4.1: Zoomed views over Dhundi of the Wishart classified maps for the (a) January 8, 2016, and (b) June 8, 2017 data. Here, only the layover and shadow mask has been applied. Also, the Kothi area is excluded from the analysis since it lies in the layover region.

443 Moreover, the Bragg surface scattering (Z3) is slightly higher in summer  
 444 (10.88%) as compared to the winter (10.38%). One plausible reason for this is  
 445 the 20 mm rainfall which occurred on June 7, 2017, evening (data retrieved from  
 446 the Dhundi record book). Also, the occurrence of fresh snowfall in areas which



447 did not have prior standing or old snow could result in surface scattering from  
448 the ground (Leinss et al., 2014). Apart from this, the asbestos gable roofs used  
449 in the human settlements (Figure 3.2(b) and Figure 3.2(d)) are strong single-  
450 bounce surface scatterers (Brunner, 2009). However, with snow accumulation  
451 on these materials, the surface scattering could be reduced. Another prominent  
452 feature noticeable in Figure 4.1(b) is the high amount of surface scattering from  
453 the river bed (Figure 3.2(c)) during the summer season. This is caused by both  
454 the boulders and the increasing flow of snow-melt water in the river (Figure  
455 3.2(c)).

456 Furthermore, the human settlements result in double-bounce scattering (Z4)  
457 (Brunner, 2009), which in the winter-time scenario reduces by 0.34%. Also, the  
458 random surface scattering (Z6) increases by 0.66% which could be caused by  
459 the presence of small snow patches on the ground. Other than this, there is  
460 a strong decrease in the low entropy multiple (dihedral) scattering from 8.23%  
461 to 5.17% in the snow-covered season which could be caused by the added snow  
462 layer on the buildings and also boulders.

463 Another interesting aspect in this context is the increase (from 9.93% to  
464 19.8%) in the number of unclassified or non-feasible pixels (Z9) for the winter-  
465 time image (Figure 4.2) which is also depicted through the  $H/\alpha$  plane plots  
466 in Figure 4.3(a) and Figure 4.3(b). This is primarily resulting from the added  
467 terrain complexity owing to the snow accumulation. In order to resolve this  
468 issue, the quad-pol entropy ( $H$ ), anisotropy ( $A \in [0, 1]$ ), alpha ( $\alpha$ ),  $H/A/\alpha$   
469 decomposition has been applied on the January 8, 2016 data. The corresponding  
470  $H/\alpha$  plane plot in Figure 4.3(c) shows that the quad-pol approach is able to  
471 fully classify the winter-time image. However, since the summer-time image  
472 is having only HH and VV channels, the dual-pol method has been used to  
473 properly compare the respective scattering mechanisms (Majumdar et al., 2019).

474 Thus, from this discussion, it is clearly observed that the presence of snow  
475 causes a substantial change of the scattering patterns in the study area resulting  
476 in significant uncertainty sources. In turn, the optimisation of the model  
477 parameters along with the sensitivity analysis of the FSD and SSD values depend

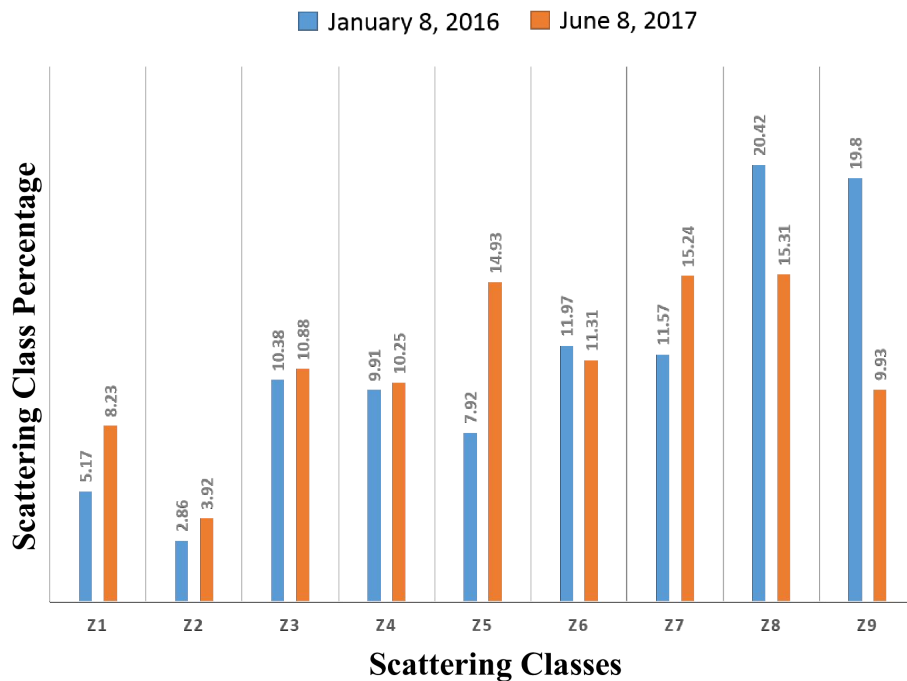


Figure 4.2: Scattering class percentages (rounded to 2 decimal places) from the unsupervised Wishart classification. The different zone labels are described in Figure 2.5.

478 on these scattering types. As an example, if there is low surface scattering then  
479 the FSD inversion model leads to underestimated values (Leinss et al., 2014)  
480 whereas for low volume scattering, the SSD results are generally underestimated  
481 (Cloude, 2005; Hajnsek et al., 2009; Kugler et al., 2015). Therefore, the  
482 uncertainty assessment by means of the scattering mechanism classification is  
483 one of the key aspects of this research.

#### 484 4.2. Sensitivity Analysis Results

485 In order to perform the sensitivity analysis, only the Dhundi area is chosen  
486 as Kothi is lying in the layover zone for this acquisition (January 8, 2016).

##### 487 4.2.1. FSD Parameters

488 The FSD inversion model discussed in section 2.2 applies the ensemble  
489 averaging operation twice—once on the computed CPD and then subsequently

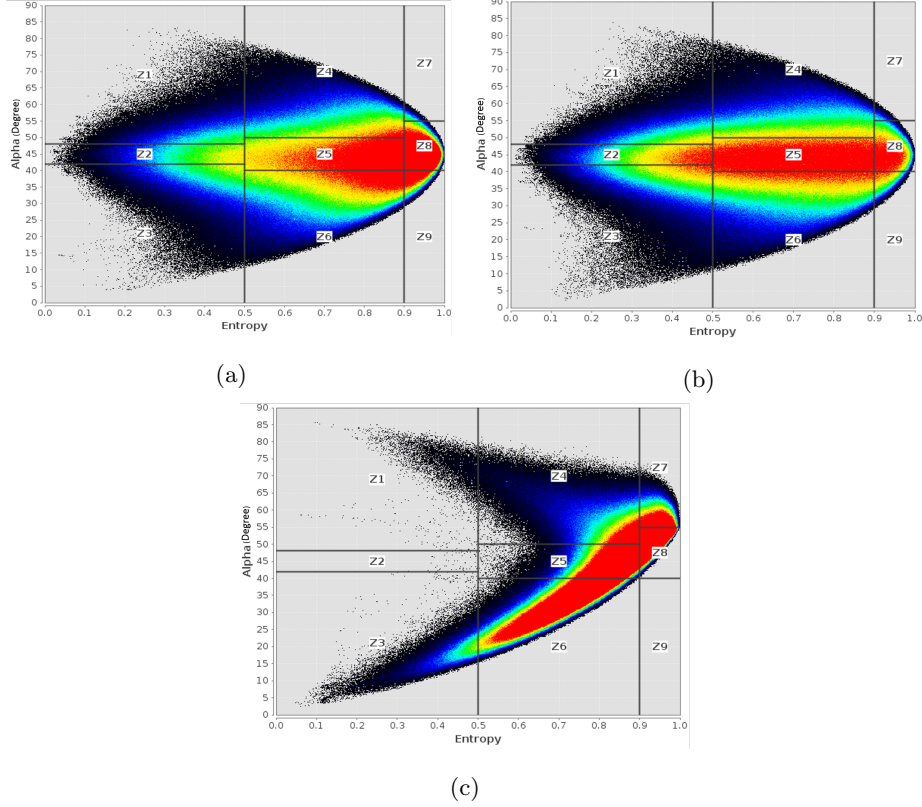


Figure 4.3: Dual-pol  $H/\alpha$  plane plots for the (a) January 8, 2016, and (b) June 8, 2017 data, (c) Quad-pol  $H/\alpha$  plane plot for the January 8, 2016 data. The colours red, green, blue, and black indicate the point density with red being the highest, and black as the lowest. These plots have been made using SNAP (ESA, 2018).

490 on the output FSD values. As a result, the selection of an optimal window size  
 491 in both these cases is critical in obtaining reliable estimates. At first, the mean  
 492 ( $\mu_{\gamma_c}$ ) and standard deviation ( $\sigma_{\gamma_c}$ ) of the copolar coherence amplitude ( $\gamma_c$ ) are  
 493 checked over the Dhundi area based on a  $3 \times 3$  neighbourhood window (same as  
 494 the validation window in section 2.4.1). The ensemble window for which the  
 495 maximum  $\mu_{\gamma_c}$  occurs is subsequently used for estimating the FSD following the  
 496 methodology described in section 2.2. This selection procedure concerning the  
 497 maximisation of  $\mu_{\gamma_c}$  is depicted in Figure 4.4 wherein the ensemble window of  
 498 size  $3 \times 3$  is found to be suitable even though  $\sigma_{\gamma_c} \approx 0.06$  of this window is slightly

499 higher than that ( $\sigma_{\gamma_c} \approx 0.02$ ) of the  $5 \times 5$  window.

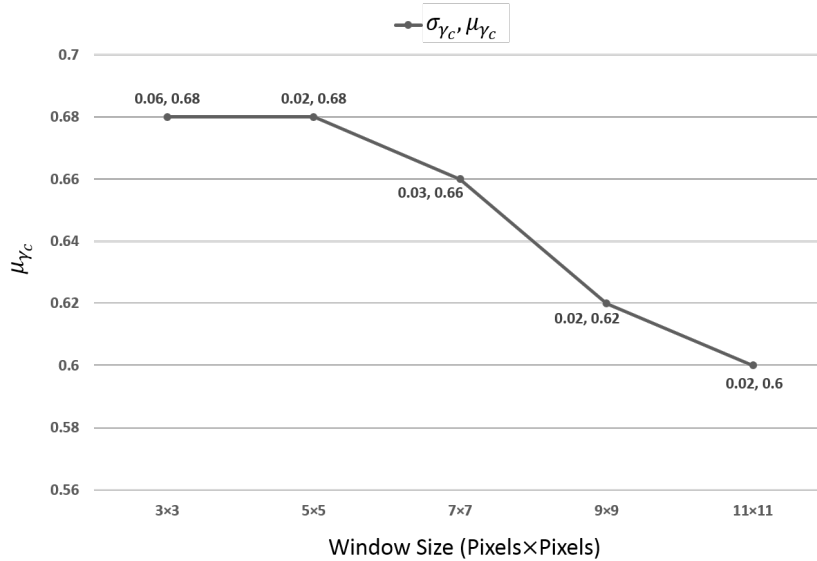


Figure 4.4: Effect of the window size on the mean and standard deviation of the copolar coherence amplitude. All the values are rounded to 2 decimal places. Here, only odd window sizes are considered because these have been previously used in prior studies (Leinss et al., 2018, 2014; Kumar & Venkataraman, 2011).

500 Next, the sensitivity of the FSD values with respect to the ensemble window  
 501 size is taken into account. This is shown in Figure 4.5 where the analysis  
 502 starts from the window size  $3 \times 3$  and continues till  $99 \times 99$  with an increment  
 503 of two pixels in each direction (Figures 4.5(a) and 4.5(b)). In this context,  
 504 smaller window sizes ( $< 45 \times 45$ ) are not considered following the work of Leinss  
 505 et al. (2014) where a  $45 \times 35$  window size has been chosen. Similarly, higher  
 506 window sizes ( $> 65 \times 65$ ) are not used because of the varying topography in the  
 507 study area. Another reason is that, since the Dhundi region exhibits moderate  
 508 undulating terrains, so from the validation perspective, window sizes which cover  
 509 ground areas of more than  $0.4 \text{ km}^2$  are excluded from the analysis. Hence, the  
 510 transect as shown in Figure 4.5(c) is used for deciding the FSD ensemble window  
 511 size.

512 In this regard, the SPA measured FSD ground-truth data at 06:22 hrs

513 January 8, 2016 (IST) was 18.7 cm, and that of the manual record book was  
514 18 cm (section 3.2). Assuming the SPA sensor bias to be 5 cm for the SD, the  
515 FSD ground observation of 18 cm is taken as the true value. Accordingly, it is  
516 observed from Figure 4.5(c) that the 65×65 window leads to the most accurate  
517 (94.83%) mean FSD ( $\mu_f \approx 18.93$  cm) with a low FSD standard deviation  
518 ( $\sigma_f \approx 0.1$  cm). The corresponding mean FSWE ( $\mu_{fs} \approx 13.25$  mm) and FSWE  
519 standard deviation ( $\sigma_{fs} \approx 0.07$  mm) are also in concordance (94.84% accuracy)  
520 with the ground-truth FSWE of 12.6 mm. However, it should be noted that  
521 the axial ratio for the fresh snow particle,  $a_x/a_z = 1.5$  is kept as an invariant  
522 throughout the entire FSD workflow (Figure 2.3) and its SA has not been carried  
523 out.

524 Here, the FSD and  $\gamma_c$  values are significantly influenced by the mixed  
525 scattering mechanisms exhibited by the ground features (Figure 4.1(a)) which  
526 are being considered for the averaging operation. Moreover, the underlying  
527 assumption of a smooth surface in the FSD inversion model does not hold  
528 for such rough terrains and consequently,  $\gamma_c$  is reduced (Leinss et al., 2014).  
529 Therefore, the FSD SA concludes that even though a sufficiently reliable FSD  
530 estimate has been achieved in the Dhundi area, the window sizes need to be  
531 adequately adjusted for different multi-temporal SAR images acquired over the  
532 same region thereby leading to a more robust parameter optimisation process.

#### 533 4.2.2. SSD Parameters

534 The SSD inversion model as described from the implementation or  
535 methodological perspective in section 2.3 incorporates several user-defined free  
536 parameters. Thus, it is necessary to conduct an appropriate SA for the hybrid  
537 Pol-InSAR based volumetric height (SSD) retrieval algorithm. Accordingly, the  
538 various model parameters and their optimisation are discussed below.

#### 539 Volume and Surface Coherence Ensemble Window

540 The ensemble windows corresponding to the number of looks (L) in Eq.  
541 (12) must be suitably chosen so as to maximise both the volume coherence

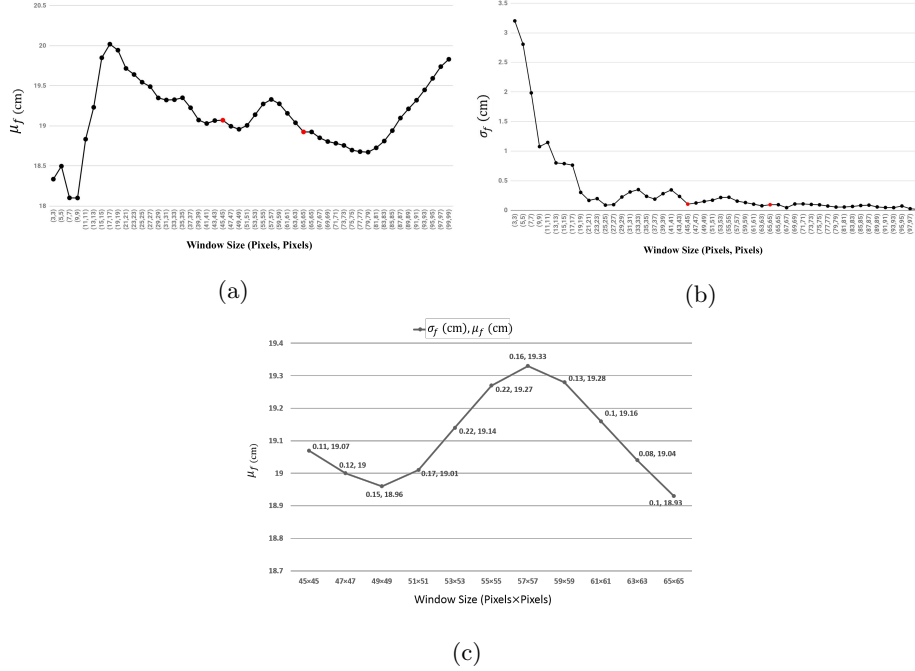


Figure 4.5: Effect of the window size on the (a) mean and (b) standard deviation of the FSD estimates. Here, the transect between the two red points ( $45 \times 45$  and  $65 \times 65$ ) are collectively shown in (c) wherein all the values are rounded to 2 decimal places.

542 amplitude,  $\gamma(\vec{w}_v)$ , and the surface coherence amplitude,  $\gamma(\vec{w}_s)$ . As a result,  
 543 the SA for these window sizes is an important aspect of this work.

544 The effects of  $L$  on the mean volume coherence amplitude,  $\mu_{\gamma(\vec{w}_v)}$  and the  
 545 mean surface coherence amplitude,  $\mu_{\gamma(\vec{w}_s)}$  which are measured by applying the  
 546 same  $3 \times 3$  neighbourhood window over Dhundi (section 2.3) along with the  
 547 respective standard deviations,  $\sigma_{\gamma(\vec{w}_v)}$  and  $\sigma_{\gamma(\vec{w}_s)}$ , are displayed in Figure 4.6.

548 It can be seen that for the executed test cases, with increasing  $L$ , there is a  
 549 general decreasing trend for both these coherences. So, for the SSD estimation,  
 550  $L = 3$  is chosen even though Cloude (2005) suggests the usage of higher values  
 551 of  $L$ . This is because,  $\sigma_{\gamma(\vec{w}_v)} \approx 0.1$  and  $\sigma_{\gamma(\vec{w}_s)} \approx 0.18$  are sufficiently small with  
 552 adequately high  $\mu_{\gamma(\vec{w}_v)} \approx 0.67$  and  $\mu_{\gamma(\vec{w}_s)} \approx 0.68$ . Also, since there is only one  
 553 validation point for the entire study area,  $L = 3$  is justifiable.

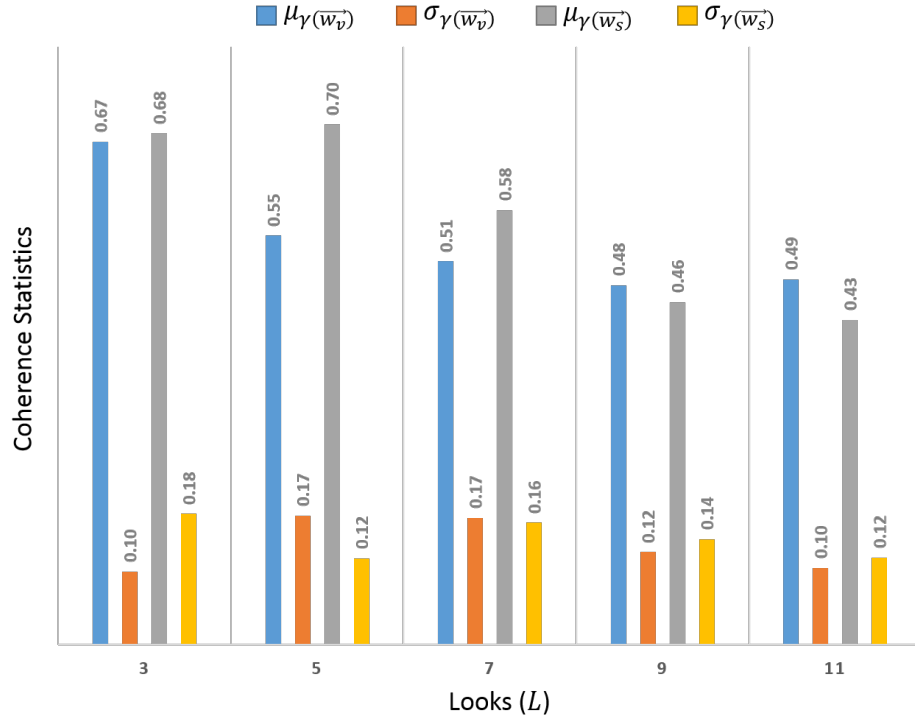


Figure 4.6: Effect of the number of looks ( $L$ ) on the volume and surface coherence. All the values are rounded to 2 decimal places.

554 However, there exist several free parameters in this Pol-InSAR based SSD  
 555 inversion model (section 2.3) and hence, the volume and surface coherence  
 556 ensemble windows need to be kept constant ( $L = 3$ ) for the subsequent SA  
 557 of the other parameters.

#### 558 *Scaling Parameters*

559 It has been previously discussed in section 2.3 that there are two scaling  
 560 parameters involved in the SSD estimation process. These are the vertical  
 561 wavenumber scaling parameter ( $\eta' \in \mathbb{R}_{>0}^+$ ) and the scaling factor ( $\eta \in [0, 1]$ )  
 562 of the hybrid DEM differencing approach developed by Cloude (2010). Here,  
 563 the SA of only  $\eta$  is carried out and  $\eta' = 5$  is kept constant throughout the  
 564 entire workflow. Also, the volume coherence threshold,  $\tau_v = 0.6$ ,  $L = 3$ , ground  
 565 phase median ensemble filter window ( $21 \times 21$ ), vertical wavenumber ensemble

566 average window ( $21 \times 21$ ), and the SSD ensemble average window of size  $57 \times 57$   
 567 are unchanged during this SA.

568 The monotonically increasing SSD with respect to increasing  $\eta$  are displayed  
 569 in Figure 4.7. For  $\eta = 0$ , the standard DEM differencing technique (Cloude,  
 570 2005) results in the mean SSD,  $\mu_s \approx 42.46$  cm with the corresponding SSD  
 571 standard deviation,  $\sigma_s \approx 0.49$  cm. As the SPA measured SSD at 06:22 hrs  
 572 IST, January 8, 2016, is 54.9 cm, so  $\mu_s$  is underestimated. Naturally, the mean  
 573 SSWE,  $\mu_{ss} \approx 133.76$  mm (with SSWE standard deviation,  $\sigma_{ss} \approx 1.53$  mm) is  
 574 also lower compared to the SPA measured SSWE of 173 mm. Thus, to effectively  
 575 optimise the volumetric height,  $\eta$  needs to be suitably increased (Cloude, 2005,  
 576 2010).

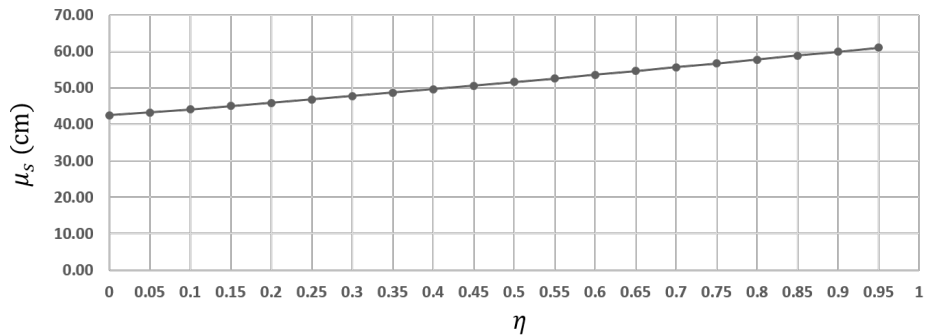


Figure 4.7: Increasing mean SSD with respect to the scaling parameter  $\eta$ .

577 In this context, Cloude (2005) has suggested setting  $\eta = 0.4$  for which the  
 578 accuracy of the estimated tree height is found to be more than 90%. Although  
 579 by keeping  $\eta = 0.4$ ,  $\mu_s \approx 49.64$  cm ( $\sigma_s \approx 0.54$  cm) is obtained with  $\sim 90.42\%$   
 580 accuracy, the complexity of the snow microstructure, anisotropy, and length  
 581 scales necessitates the need for achieving even higher accuracies (Leinss et al.,  
 582 2016). Moreover, in the presence of significantly varying hydrometeorological  
 583 conditions which include high surface roughness and associated uncertainty  
 584 sources (section 4.1), the volume and surface coherence amplitudes generally do  
 585 not reach expected values of higher than 0.8 (Cloude, 2005; Kugler et al., 2015).  
 586 Therefore, with  $\eta = 0.65$ , the best SSD and SSWE accuracies of 99.53% ( $\mu_s \approx$



587 54.64 cm) and 99.48% ( $\mu_{ss} \approx 172.10$  mm) respectively are achieved over Dhundi  
 588 with low standard deviations ( $\sigma_s \approx 0.58$  cm,  $\sigma_{ss} \approx 1.82$  mm) accounting for  
 589 high reliability. These results highlight the significance of this scaling parameter  
 590  $\eta$  towards controlling the snow structural height variations (Cloude, 2005, 2010)  
 591 and hence, the robustness of the hybrid DEM differencing model (section 2.3)  
 592 is verified.

593 *Computing sinc Inverse*

594 In order to test the accuracy of the  $\text{sinc}_\pi$  inverse function, sample test data  
 595 representing the actual inverse,  $\alpha_r$ , have been prepared as shown in Table  
 596 4.1. Next, the  $\text{sinc}_\pi$  of these data,  $\text{sinc}_\pi(\alpha_r)$ , is computed which essentially  
 597 corresponds to the possible  $\gamma(\vec{w}_v)$  values. So, the idea of performing SA in this  
 598 scenario is to check the accuracy of the calculated  $\text{sinc}_{\pi_C}^{-1}$  (Eq. (2.11c)) and  
 599  $\text{sinc}_{\pi_S}^{-1}$  (Eq. (2.11b)) of the  $\text{sinc}_\pi(\alpha_r)$  values by comparing these with  $\alpha_r$ .

Table 4.1: Comparison between the normalised Cloude (2010) sinc inverse and the secant sinc inverse methods.

$\alpha_r$ (rad)	$\text{sinc}_\pi(\alpha_r)$	$\text{sinc}_{\pi_C}^{-1}$ (rad)	$\text{sinc}_{\pi_S}^{-1}$ (rad)
0.1	0.984	0.103	0.100
0.2	0.935	0.206	0.200
0.3	0.858	0.308	0.300
0.4	0.757	0.409	0.400
0.5	0.637	0.509	0.500
0.6	0.505	0.607	0.600
0.7	0.368	0.703	0.700
0.8	0.234	0.798	0.800
0.9	0.109	0.891	0.900

600 From Table 4.1 it is observed that the secant method converges exactly  
 601 (up to 13 decimal places) to the actual  $\alpha_r$ , while the normalised Cloude (2010)  
 602 approximation of the  $\text{sinc}_\pi$  inverse has some minute errors involved (RMSE  $\approx$   
 603 0.02 rad). Similarly, the sinc function is tested (Table 4.2) where  $\text{sinc}_C^{-1}$  and

604  $\text{sinc}_S^{-1}$  denote the standard [Cloude \(2010\)](#) approximation (Eq. (2.11a)) and  
 605 the secant method of root finding for the traditional sinc function respectively.  
 606 Again, the secant method exactly converges (up to 13 decimal places) whereas  
 607 RMSE  $\approx 0.02$  rad is associated with the  $\text{sinc}_C^{-1}$ . Here, the computed results  
 608 shown in Table 4.1 and Table 4.2 are rounded to 3 decimal places.

Table 4.2: Comparison between the traditional [Cloude \(2010\)](#) sinc inverse and the secant sinc inverse methods.

$\alpha_r$ (rad)	$\text{sinc}(\alpha_r)$	$\text{sinc}_C^{-1}$ (rad)	$\text{sinc}_S^{-1}$ (rad)
0.1	0.998	0.103	0.100
0.2	0.993	0.207	0.200
0.3	0.985	0.310	0.300
0.4	0.974	0.413	0.400
0.5	0.959	0.516	0.500
0.6	0.941	0.618	0.600
0.7	0.920	0.721	0.700
0.8	0.897	0.823	0.800
0.9	0.870	0.925	0.900

609 Therefore, by performing the SA of the  $\text{sinc}_{\pi_C}^{-1}$ ,  $\text{sinc}_{\pi_S}^{-1}$ ,  $\text{sinc}_C^{-1}$ , and  $\text{sinc}_S^{-1}$ , it  
 610 is clearly understood that the secant method provides highly accurate results.  
 611 Hence, in this work,  $\text{sinc}_{\pi_S}^{-1}$  is applied for solving Eq. (2.9a) wherein the  
 612  $\text{sinc}_{\pi_C}^{-1}(\gamma(\vec{w}_v))$  value is used as an initial guess to the secant method for faster  
 613 convergence.

#### 614 *SSD Ensemble Window*

615 Another essential free parameter used in the Pol-InSAR based SSD  
 616 estimation model (section 2.3) is the SSD ensemble averaging window size. By  
 617 keeping  $\eta = 0.65$ ,  $\eta' = 5$ , and other ensemble window sizes constant, the SA has  
 618 been carried out to observe the SSD variations which are shown in Figure 4.8.  
 619 Here, the ensemble windows are the same which have been previously applied

620 for the FSD values (section 4.2.1) so as to appropriately compare the SSD and  
 621 FSD estimates.

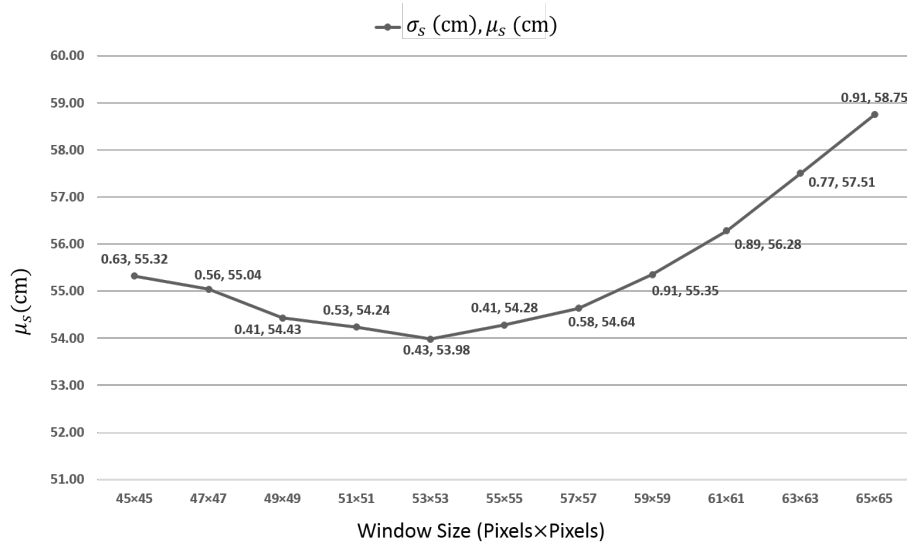


Figure 4.8: Effect of the ensemble window size on the SSD values.

622 The graphical representation in Figure 4.8 shows that when the window size  
 623 is increased beyond 57×57, the SSD values increase sharply whereas, between  
 624 the windows 53×53 and 57×57, the values are mostly similar. This could be  
 625 attributed by the fact that, in mountainous terrains, elevation, and not distance,  
 626 plays a critical role in controlling the snow accumulation (Liu et al., 2017; Singh  
 627 et al., 2014, 2017; Thakur et al., 2012). The varying topographical conditions  
 628 prominently visible in Figure 3.2 also ascertain that for larger window sizes, the  
 629 snow depth variability could increase if a nearby mountain also lies within the  
 630 neighbourhood window. So, considering these aspects, the ensemble window  
 631 size of 57×57 is selected which results in  $\mu_s \approx 54.64$  cm with  $\sigma_s \approx 0.58$  cm as  
 632 discussed in the scaling parameter SA.

#### 633 4.2.3. DEM and LIA Error Analysis

634 During the field visit (section 3.1.2), several DGPS points which had been  
 635 acquired are used to check the accuracy of the ALOS PALSAR DEM. In essence,

636 the observed errors are then used to analyse the change in the LIA (Eq. (2.12))  
637 induced by the corrected DEM (the erroneous DEM pixels are replaced by the  
638 respective DGPS measurements).

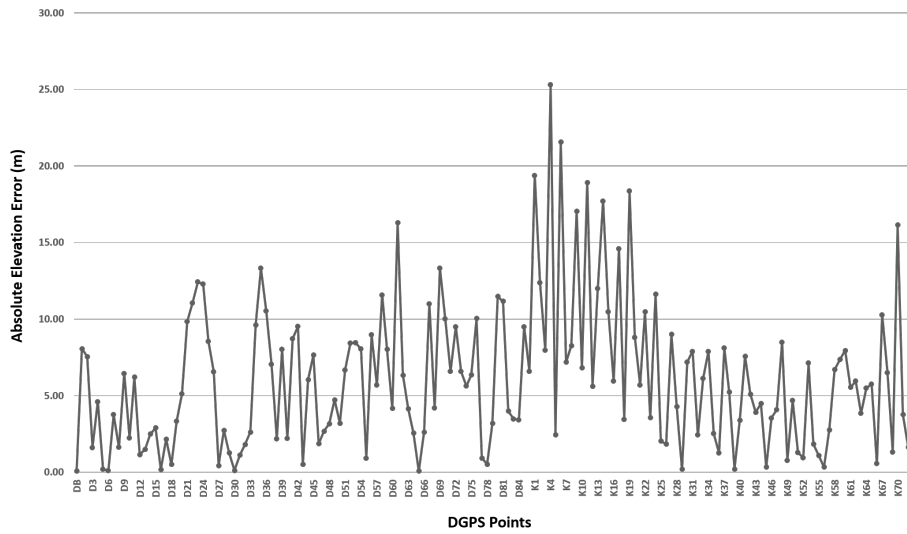
639 The DEM errors calculated using the Dhundi and Kothi DGPS readings are  
640 displayed in Figure 4.9(a) and the subsequent LIA differences (computed from  
641 the corrected and original DEMs) for these points are shown in Figure 4.9(b).  
642 As seen from these graphs, the absolute elevation errors range from 0.08 m  
643 to 16.30 m in the Dhundi region, whereas these vary from 0.19 m to 25.32 m  
644 in the Kothi area. Accordingly, the RMSE values for the elevation errors are  
645 approximately 6.71 m and 8.8 m respectively.

646 In addition, the LIA varies from  $0^\circ$  to  $7.59^\circ$  (Dhundi) and  $0^\circ$  to  $0.17^\circ$  (Kothi)  
647 in these areas with the corresponding RMSE being nearly  $2.54^\circ$  and  $0.02^\circ$ .  
648 However, since the LIA is dependent on the slope values (Eq. (2.12)), the  
649 DEM errors do not significantly influence the LIA. Also, in the FSD inversion  
650 model and the vertical wavenumber calculation (used in the SSD estimation)  
651 given by Eq. (2.7) and Eq. (2.9b) respectively, the sine (sin) of the LIA  
652 is considered. So, the minute changes in the LIA do not strongly affect the  
653 FSD and SSD estimates which are obtained after applying sufficient ensemble  
654 averaging operation (section 2). Evidently, the LIA only changes by about  
655  $1.9^\circ$  near the Dhundi base station and thus, the FSD and SSD results are not  
656 exhibiting any sizeable impact from the associated DEM errors.

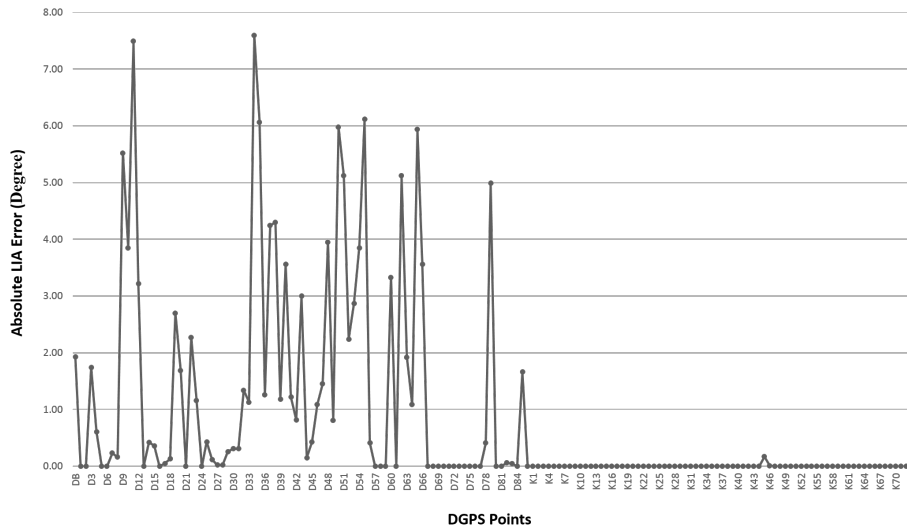
657 Therefore, the SA concerning the DEM errors and its propagation highlights  
658 that the subsequent LIA errors are not directly governed by the changes in the  
659 elevation values, rather the slopes in  $x$  and  $y$  directions (section 2.4.3) act as the  
660 primary error sources. Also, the ALOS PALSAR DEM is sufficiently accurate  
661 even in the complex terrains and hence, its usage in the LIA computation is  
662 justified.

#### 663 4.3. Comparative Analysis of the Estimates

664 In order to visually observe the spatial patterns of the FSD and SSD  
665 estimates, suitable maps have been prepared which are shown in Figure 4.10(a)



(a)



(b)

Figure 4.9: (a) Absolute DEM errors obtained by comparing ALOS PALSAR DEM and the DGPS measurements and (b) observed absolute LIA errors. Here DB is the Dhundi base station point, D1-D86 are acquired in the Dhundi region, and K1-K72 are measured in the Kothi area using the DGPS.

666 and Figure 4.10(b) respectively. Here, the resultant FSWE and SSWE maps  
 667 are not shown as these have been computed by multiplying the constant snow  
 668 densities,  $\rho_f = 0.07 \text{ g/cm}^3$  and  $\rho_s = 0.315 \text{ g/cm}^3$  to the FSD and SSD values  
 669 respectively. Therefore, they have similar spatial characteristics like those of  
 670 the snow depth maps.

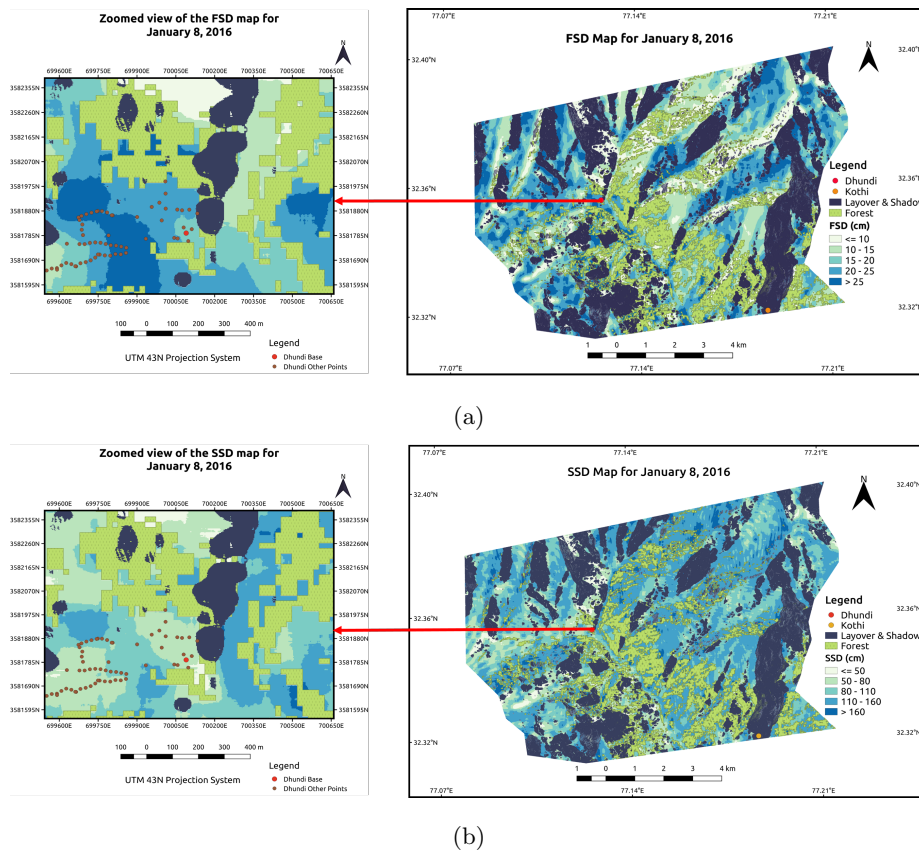


Figure 4.10: Zoomed views of the (a) FSD map and (b) SSD map for January 8, 2016. Here, the ground points surveyed (section 3.1.2) are shown wherein the closely spaced points have been acquired using the DGPS kinematic mode and fall on the nearby roads in the Dhundi region. The other points including the Dhundi base are measured using the static mode. Since the Kothi area falls in the layover and shadow zone, it is excluded from the zoomed view analysis.

671 As discussed earlier in sections 4.2.1 and 4.2.2, the optimal FSD and SSD

672 ensemble window sizes are  $65 \times 65$  and  $57 \times 57$  respectively. The maps in Figure  
673 4.10 show these ensemble averaged estimates wherein  $\mu_f \approx 18.93 \pm 5.03$  cm  
674 ( $\sigma_f \approx 0.1$  cm) and  $\mu_s \approx 54.64 \pm 5.19$  cm ( $\sigma_s \approx 0.58$  cm) are observed  
675 over the  $3 \times 3$  neighbourhood window surrounding the Dhundi area with the  
676 corresponding  $\mu_{fs} \approx 13.25 \pm 5.02$  mm ( $\sigma_{fs} \approx 0.07$  mm) and  $\mu_{ss} \approx 172.10 \pm$   
677  $5.61$  mm ( $\sigma_{ss} \approx 1.82$  mm). Here, the uncertainties are calculated based on the  
678 standard error of the estimate and the SPA measurement biases of 5 cm and 5  
679 mm for the SD and SWE have been assumed respectively.

680 In addition, the overall mean FSD and SSD are 17.90 cm and 112.17 cm  
681 respectively wherein the standard deviations are found to be  $\sim 6.46$  cm and  
682  $\sim 30.80$  cm. Accordingly, the mean FSWE and SSWE are  $\sim 12.12$  mm and  
683  $\sim 377.81$  mm respectively where the associated standard deviations are  $\sim 4.46$   
684 mm and  $\sim 101.55$  mm.

685 The high SSD and SSWE standard deviations for the complete region  
686 highlight the extreme topographical conditions present in the study area. These  
687 variations can be confirmed from the ground survey (section 3.1.2) where the  
688 points (shown in Figure 4.10) had been acquired by considering the terrain  
689 undulations. Also, the aspect, slope, and elevation significantly influence the  
690 FSD and SSD estimates, the details of which have been discussed in the previous  
691 section.

692 Apart from this, it can be observed that these estimates are lower in  
693 the Dhundi base station area as compared to the surrounding regions. This  
694 phenomenon can be attributed to the presence of the human settlements (Figure  
695 3.2(b)) near the base point and are expected to have less snow accumulation  
696 than the natural surroundings. Moreover, the effect of multiple or double  
697 bounce scattering (Z4) near the Dhundi base is prominent even during the winter  
698 (Figure 4.1(a)). So, this could effectively reduce the copolar, volume and surface  
699 coherences (sections 4.2.1 and 4.2.2) thereby explaining this observation.

700 **5. Conclusion and Future Scope**

701 The primary focus of this research lies in estimating the snow depth using  
702 which the snow water equivalent has been measured. Here, two different types  
703 of snow have been considered freshly fallen (new) snow and standing (old) snow.  
704 In order to compute the FSD, the CPD method has been applied (section 2.2)  
705 on the January 8, 2016, TSX-TDX CoSSC bistatic dataset acquired over the  
706 Beas watershed, northwestern Himalayas (section 3). Additionally, the hybrid  
707 DEM differencing and coherence amplitude inversion algorithm based on the  
708 single-baseline Pol-InSAR technique has been utilised to estimate the SSD for  
709 the same dataset (section 2.3). Also, the corresponding FSWE and SSWE are  
710 obtained by multiplying constant fresh and standing snow densities.

711 Due to the complex hydrometeorological and topographical conditions of the  
712 study area (section 3.1.1), significant uncertainty sources are present. These  
713 include the forests, boulders, highly rough surfaces, and human settlements  
714 (Figure 3.2) which substantially reduce the surface and volume scattering  
715 coherences required to estimate the snow depths with adequate accuracy  
716 (2.4). Moreover, the limited ground-truth data availability has always been  
717 a major challenge from the onset of this work (section 3.2). Apart from  
718 this, the SAR data are affected by layover, shadowing and foreshortening in  
719 mountainous terrains and hence, these errors are inherently propagated through  
720 the subsequent processing steps. Furthermore, the PolSAR and Pol-InSAR  
721 models involve several user-defined parameters which have to be optimised  
722 (section 2). In short, these are the main concerns involved in this work  
723 which are addressed by means of identifying the potential uncertainty sources  
724 ( $H/\alpha$  decomposition and Wishart classification) and performing appropriate  
725 sensitivity analysis (section 2.4.3).

726 Thus, the novelty of this research lies in suitably modifying and ultimately  
727 improving the hybrid Pol-InSAR model (section 2.3) to estimate the SSD which  
728 is new in the context of cryospheric studies. Additionally, the PolSAR CPD  
729 method for FSD retrieval has been tested for the first time in the presence



730 of extreme topographically varying conditions. Although the FSD and SSD  
731 ground-truth measurements from only the Dhundi station had been available,  
732 the high accuracies of 94.83% and 99.53% respectively imply that these improved  
733 models work sufficiently well under the complex hydrometeorological situations.

734 As part of future work, it is recommended to use the multi-baseline Pol-  
735 InSAR technique (Cloude, 2010) wherein  $k_z$  can be simulated (instead of scaling  
736 by  $\eta'$ ) after an appropriate accuracy assessment (Kumar et al., 2017). Similarly,  
737 the effect of different window shapes (square or rectangular) and sizes can be  
738 considered for the ensemble averaging operation. This sort of sensitivity analysis  
739 will help in deciding optimal window structures separately for each model.  
740 Moreover, it is recommended to apply scattering mechanism based masks in  
741 conjunction with snow masks prepared from the high resolution optical datasets  
742 such as those provided by Sentinel-2 (Zhu et al., 2015). Additionally, the prior  
743 classification of the dry and wet snow including the preparation of snow cover  
744 maps (Leinss et al., 2018; Thakur et al., 2012; Zhu et al., 2015) as necessary  
745 preprocessing steps will certainly improve the uncertainty assessment process.

746 Also, the use of the newer multi-temporal high resolution L-band datasets  
747 acquired by the upcoming SAR missions (Tridon et al., 2018; Rosen et al., 2017)  
748 is recommended to further verify and validate these models. Moreover, radar  
749 altimeters such as the Ka-band InSAR altimeter could potentially improve the  
750 SD and SWE estimates, and could also be used for operational snow depth  
751 monitoring on a large-scale (Hensley et al., 2016; Kim et al., 2018; Moller et al.,  
752 2011; Speziali et al., 2018).

753 In this work, one dataset (January 8, 2016) was used for analysis. Preferably,  
754 if a full scale time series analysis is performed, then the robustness of the SSD  
755 and FSD retrieval models can be checked. Furthermore, Pol-InSAR coherency  
756 optimisation can be carried out to suitably adjust the scattering phase centres  
757 (Cloude, 2005, 2010). Moreover, the snow densities need to be computed  
758 gridwise (or if possible, pixelwise) by using hydrological modelling approaches  
759 (Bartelt & Lehning, 2002; Liang et al., 1994). These can also be estimated from  
760 the PolSAR based techniques which are in practice (Singh et al., 2017; Thakur

761 [et al., 2012](#)). Finally, appropriate statistical significance testing needs to be  
762 carried out to quantify further the uncertainties associated with the FSD and  
763 SSD estimates.

#### 764 **Acknowledgements**

765 This research work was carried out as part of the ISRO EOAM mountain  
766 ecosystem, TANDEM-X AO and ALOS-RA4 project (EOAM-ME (WRD))  
767 on the Himalayan glaciers. Also, this work was conducted within the IIRS,  
768 ISRO and University of Twente, Faculty ITC joint education programme  
769 (JEP) framework. The authors are grateful to IIRS, ISRO, University of  
770 Twente, Faculty ITC along with SASE, DRDO and the FOSS4G community  
771 for providing the necessary means to conduct this study.

#### 772 **References**

- 773 Abe, T., Yamaguchi, Y., & Sengoku, M. (1990). Experimental study of  
774 microwave transmission in snowpack. *IEEE Trans. Geosci. Remote Sens.*,  
775 *28*, 915–921. doi:[10.1109/36.58981](https://doi.org/10.1109/36.58981).
- 776 Balss, U., Breit, H., Duque, S., Fritz, T., & Rossi, C. (2012). *CoSSC Generation*  
777 *and Interferometric Considerations (TD-PGS-TN-3129)*. Technical Report  
778 Remote Sensing Technology Institute, DLR Oberpfaffenhofen, Germany.  
779 URL: [https://tandemx-science.dlr.de/pdfs/TD-PGS-TN-3129\\_](https://tandemx-science.dlr.de/pdfs/TD-PGS-TN-3129_CoSSCGenerationInterferometricConsiderations_1.0.pdf)  
780 [CoSSCGenerationInterferometricConsiderations\\_1.0.pdf](https://tandemx-science.dlr.de/pdfs/TD-PGS-TN-3129_CoSSCGenerationInterferometricConsiderations_1.0.pdf).
- 781 Bartelt, P., & Lehning, M. (2002). A physical SNOWPACK model for the  
782 Swiss avalanche warning. *Cold Reg. Sci. Technol.*, *35*, 123–145. doi:[10.1016/](https://doi.org/10.1016/S0165-232X(02)00074-5)  
783 [S0165-232X\(02\)00074-5](https://doi.org/10.1016/S0165-232X(02)00074-5).
- 784 Brunner, D. (2009). *Advanced Methods For Building Information Extraction*  
785 *From Very High Resolution SAR Data To Support Emergency Response*.  
786 Doctoral thesis Trento: University of Trento. URL: [http://eprints-phd.](http://eprints-phd.biblio.unitn.it/233/1/PHD_Thesis_Dominik_Brunner.pdf)  
787 [biblio.unitn.it/233/1/PHD\\_Thesis\\_Dominik\\_Brunner.pdf](http://eprints-phd.biblio.unitn.it/233/1/PHD_Thesis_Dominik_Brunner.pdf).

- 788 Cheney, E. W., & Kincaid, D. R. (2012). Nonlinear equations. In *Numer. Math.*  
789 *Comput.* (pp. 114–150). Boston, USA: Cengage Learning. (7th ed.).
- 790 Cloude, S. R. (2005). *POL-InSAR training course*. Technical  
791 Report ESA. URL: [https://earth.esa.int/landtraining07/pol-insar\\_](https://earth.esa.int/landtraining07/pol-insar_training_course.pdf)  
792 [training\\_course.pdf](https://earth.esa.int/landtraining07/pol-insar_training_course.pdf).
- 793 Cloude, S. R. (2010). *Polarisation: Applications in Remote Sensing*. New  
794 York: Oxford University Press. doi:[10.1093/acprof:oso/9780199569731.](https://doi.org/10.1093/acprof:oso/9780199569731.001.0001)  
795 [001.0001](https://doi.org/10.1093/acprof:oso/9780199569731.001.0001).
- 796 Conde, V., Nico, G., Mateus, P., Catalão, J., Kontu, A., & Gritsevich, M.  
797 (2019). On The Estimation of Temporal Changes of Snow Water Equivalent  
798 by Spaceborne Sar Interferometry: A New Application for the Sentinel-1  
799 Mission. *J. Hydrol. Hydromechanics*, *67*. doi:[10.2478/johh-2018-0003](https://doi.org/10.2478/johh-2018-0003).
- 800 Deems, J. S., Painter, T. H., & Finnegan, D. C. (2013). Lidar measurement of  
801 snow depth: a review. *J. Glaciol.*, *59*, 467–479. doi:[10.3189/2013JoG12J154](https://doi.org/10.3189/2013JoG12J154).
- 802 ESA (2018). SNAP. URL: <http://step.esa.int/main/toolboxes/snap/>.
- 803 Guneriusson, T., Høgda, K. A., Johnsen, H., & Lauknes, I. (2001). InSAR for  
804 estimation of changes in snow water equivalent of dry snow. *IEEE Trans.*  
805 *Geosci. Remote Sens.*, *39*, 2101–2108. doi:[10.1109/36.957273](https://doi.org/10.1109/36.957273).
- 806 Hajnsek, I., Kugler, F., Lee, S.-K., & Papathanassiou, K. P. (2009). Tropical-  
807 Forest-Parameter Estimation by Means of Pol-InSAR: The INDREX-II  
808 Campaign. *IEEE Trans. Geosci. Remote Sens.*, *47*, 481–493. doi:[10.1109/](https://doi.org/10.1109/TGRS.2008.2009437)  
809 [TGRS.2008.2009437](https://doi.org/10.1109/TGRS.2008.2009437).
- 810 Hanssen, R. F. (2001). *Radar Interferometry - Data Interpretation and*  
811 *Error Analysis* volume 2 of *Remote Sensing and Digital Image Processing*.  
812 Dordrecht: Kluwer Academic Publishers. doi:[10.1007/0-306-47633-9](https://doi.org/10.1007/0-306-47633-9).
- 813 Hensley, S., Moller, D., Oveisgharan, S., Michel, T., & Wu, X. (2016). Ka-Band  
814 Mapping and Measurements of Interferometric Penetration of the Greenland

- 815 Ice Sheets by the GLISTIN Radar. *IEEE J. Sel. Top. Appl. Earth Obs.*  
816 *Remote Sens.*, 9, 2436–2450. doi:10.1109/JSTARS.2016.2560626.
- 817 Hoen, E. W., & Zebker, H. (2000). Penetration depths inferred from  
818 interferometric volume decorrelation observed over the Greenland Ice Sheet.  
819 *IEEE Trans. Geosci. Remote Sens.*, 38, 2571–2583. doi:10.1109/36.885204.
- 820 JetBrains (2018). PyCharm Documentation. URL: <https://www.jetbrains.com/pycharm/documentation/index.html>.  
821
- 822 Jones, E., Oliphant, E., & Peterson, P. (2001). SciPy: Open Source Scientific  
823 Tools for Python. URL: <http://www.scipy.org/>.
- 824 Kim, E. J., Gatebe, C. K., Hall, D. K., & Kang, D. H. (2018). *NASA's SnowEx*  
825 *Campaign and Measuring Global Snow from Space (GSFC-E-DAA-TN55784)*.  
826 Technical Report NASA Pyeongchang, Republic of Korea. URL: <https://ntrs.nasa.gov/search.jsp?R=20180005187>.  
827
- 828 Kugler, F., Lee, S.-K., Hajnsek, I., & Papathanassiou, K. P. (2015). Forest  
829 Height Estimation by Means of Pol-InSAR Data Inversion: The Role of the  
830 Vertical Wavenumber. *IEEE Trans. Geosci. Remote Sens.*, 53, 5294–5311.  
831 doi:10.1109/TGRS.2015.2420996.
- 832 Kumar, S., Khati, U. G., Chandola, S., Agrawal, S., & Kushwaha, S. P.  
833 (2017). Polarimetric SAR Interferometry based modeling for tree height and  
834 aboveground biomass retrieval in a tropical deciduous forest. *Adv. Sp. Res.*,  
835 60, 571–586. doi:10.1016/j.asr.2017.04.018.
- 836 Kumar, V., & Venkataraman, G. (2011). SAR interferometric coherence analysis  
837 for snow cover mapping in the western Himalayan region. *Int. J. Digit. Earth*,  
838 4, 78–90. doi:10.1080/17538940903521591.
- 839 Lee, J.-S., & Pottier, E. (2009). *Polarimetric Radar Imaging: From Basics to*  
840 *Applications*. Boca Raton, Florida, USA: CRC Press. URL: <https://www.taylorfrancis.com/books/9781420054972>.  
841

- 842 Lee, J.-S., Schuler, D. L., & Ainsworth, T. L. (2000). Polarimetric SAR  
843 data compensation for terrain azimuth slope variation. *IEEE Trans. Geosci.*  
844 *Remote Sens.*, *38*, 2153–2163. doi:[10.1109/36.868874](https://doi.org/10.1109/36.868874).
- 845 Leica Geosystems AG (2012). *Leica GS10/GS15 User Manual (772916-*  
846 *4.1.0en)*. Technical Report Leica Geosystems AG Heerbrugg, Switzerland.  
847 URL: [http://www.surveyequipment.com/PDFs/Leica\\_Viva\\_GS10\\_GS15\\_](http://www.surveyequipment.com/PDFs/Leica_Viva_GS10_GS15_User_Manual.pdf)  
848 [User\\_Manual.pdf](http://www.surveyequipment.com/PDFs/Leica_Viva_GS10_GS15_User_Manual.pdf).
- 849 Leinss, S., Antropov, O., Vehvilainen, J., Lemmetyinen, J., Hajnsek, I., &  
850 Praks, J. (2018). Wet Snow Depth from Tandem-X Single-Pass Insar Dem  
851 Differencing. In *IGARSS 2018 - 2018 IEEE Int. Geosci. Remote Sens. Symp.*  
852 (pp. 8500–8503). IEEE. doi:[10.1109/IGARSS.2018.8518661](https://doi.org/10.1109/IGARSS.2018.8518661).
- 853 Leinss, S., Löwe, H., Proksch, M., Lemmetyinen, J., Wiesmann, A., &  
854 Hajnsek, I. (2016). Anisotropy of seasonal snow measured by polarimetric  
855 phase differences in radar time series. *The Cryosphere*, *10*, 1771–1797.  
856 doi:[10.5194/tc-10-1771-2016](https://doi.org/10.5194/tc-10-1771-2016).
- 857 Leinss, S., Parrella, G., & Hajnsek, I. (2014). Snow height determination by  
858 polarimetric phase differences in X-Band SAR Data. *IEEE J. Sel. Top. Appl.*  
859 *Earth Obs. Remote Sens.*, *7*, 3794–3810. doi:[10.1109/JSTARS.2014.2323199](https://doi.org/10.1109/JSTARS.2014.2323199).
- 860 Leinss, S., Wiesmann, A., Lemmetyinen, J., & Hajnsek, I. (2015). Snow Water  
861 Equivalent of Dry Snow Measured by Differential Interferometry. *IEEE J. Sel.*  
862 *Top. Appl. Earth Obs. Remote Sens.*, *8*, 3773–3790. doi:[10.1109/JSTARS.](https://doi.org/10.1109/JSTARS.2015.2432031)  
863 [2015.2432031](https://doi.org/10.1109/JSTARS.2015.2432031).
- 864 Li, H., Wang, Z., He, G., & Man, W. (2017). Estimating Snow Depth and Snow  
865 Water Equivalence Using Repeat-Pass Interferometric SAR in the Northern  
866 Piedmont Region of the Tianshan Mountains. *J. Sensors*, *2017*, 1–17. doi:[10.](https://doi.org/10.1155/2017/8739598)  
867 [1155/2017/8739598](https://doi.org/10.1155/2017/8739598).
- 868 Liang, X., Lettenmaier, D. P., Wood, E. F., & Burges, S. J. (1994). A  
869 simple hydrologically based model of land surface water and energy fluxes

- 870 for general circulation models. *J. Geophys. Res.*, *99*, 14415–14428. doi:10.  
871 [1029/94JD00483](https://doi.org/10.1029/94JD00483).
- 872 Liu, Y., Li, L., Yang, J., Chen, X., & Hao, J. (2017). Estimating snow depth  
873 using multi-source data fusion based on the D-InSAR method and 3DVAR  
874 fusion algorithm. *Remote Sens.*, *9*. doi:10.3390/rs9111195.
- 875 Luo, X., Richter, B., & Cole, A. (2014). *GLONASS only and BeiDou*  
876 *only RTK Positioning*. Technical Report Leica Geosystems AG  
877 Heerbrugg, Switzerland. URL: [https://leica-geosystems.com/-/media/  
878 Files/LeicaGeosystems/Products/WhitePapers/GLONASS\\_BeiDou\\_RTK\\_  
879 Positioning\\_WPA.ashx](https://leica-geosystems.com/-/media/Files/LeicaGeosystems/Products/WhitePapers/GLONASS_BeiDou_RTK_Positioning_WPA.ashx).
- 880 Majumdar, S., Thakur, P. K., Chang, L., & Kumar, S. (2019). X-  
881 band Polarimetric SAR Copolar Phase Difference for Fresh Snow Depth  
882 Estimation in the Northwestern Himalayan Watershed. URL: [https:  
883 //igarss2019.org/Papers/ViewPapers.asp?PaperNum=3115](https://igarss2019.org/Papers/ViewPapers.asp?PaperNum=3115) accepted in  
884 2019 IEEE International Geoscience and Remote Sensing Symposium  
885 (IGARSS 2019), Yokohama, Japan.
- 886 Moller, D., Hensley, S., Sadowy, G. A., Fisher, C. D., Michel, T., Zawadzki,  
887 M., & Rignot, E. (2011). The Glacier and Land Ice Surface Topography  
888 Interferometer: An Airborne Proof-of-Concept Demonstration of High-  
889 Precision Ka-Band Single-Pass Elevation Mapping. *IEEE Trans. Geosci.*  
890 *Remote Sens.*, *49*, 827–842. doi:10.1109/TGRS.2010.2057254.
- 891 Moreira, A., Prats-Iraola, P., Younis, M., Krieger, G., Hajnsek, I., &  
892 Papathanassiou, K. P. (2013). A tutorial on synthetic aperture radar. *IEEE*  
893 *Geosci. Remote Sens. Mag.*, *1*, 6–43. doi:10.1109/MGRS.2013.2248301.
- 894 Papathanassiou, K., & Cloude, S. (2001). Single-baseline polarimetric SAR  
895 interferometry. *IEEE Trans. Geosci. Remote Sens.*, *39*, 2352–2363. doi:10.  
896 [1109/36.964971](https://doi.org/10.1109/36.964971).

- 897 Parrella, G., Hajnsek, I., & Papathanassiou, K. P. (2013). On the Interpretation  
898 of L- and P-Band PolSAR Signatures of Polythermal Glaciers. In *6th Int.*  
899 *Work. Sci. Appl. SAR Polarim. Polarim. Interferom.* (pp. 1–6). Frascati,  
900 Italy. URL: [https://elib.dlr.de/78902/1/s7\\_parre.pdf](https://elib.dlr.de/78902/1/s7_parre.pdf).
- 901 PostgreSQL (2019). PostgreSQL. URL: <https://www.postgresql.org/>.
- 902 QGIS (2016). Changelog for QGIS 2.18. URL: [https://www.qgis.org/en/  
903 site/forusers/visualchangelog218/index.html](https://www.qgis.org/en/site/forusers/visualchangelog218/index.html).
- 904 Reynolds, B. (1983). The chemical composition of snow at a rural upland site  
905 in Mid-wales. *Atmos. Environ.*, *17*, 1849–1851. doi:10.1016/0004-6981(83)  
906 90193-2.
- 907 Riche, F., Montagnat, M., & Schneebeli, M. (2013). Evolution of crystal  
908 orientation in snow during temperature gradient metamorphism. *J. Glaciol.*,  
909 *59*, 47–55. doi:10.3189/2013Jog12J116.
- 910 Rosen, P., Hensley, S., Shaffer, S., Edelstein, W., Kim, Y., Kumar, R., Misra, T.,  
911 Bhan, R., & Sagi, R. (2017). The NASA-ISRO SAR (NISAR) mission dual-  
912 band radar instrument preliminary design. In *2017 IEEE Int. Geosci. Remote*  
913 *Sens. Symp.* (pp. 3832–3835). IEEE. doi:10.1109/IGARSS.2017.8127836.
- 914 Sihvola, A. (1999). *Electromagnetic Mixing Formulas and Applications*. (1st  
915 ed.). UK: The Institution of Engineering and Technology. doi:10.1049/  
916 PBEW047E.
- 917 Singh, G., Venkataraman, G., Yamaguchi, Y., & Park, S.-E. (2014). Capability  
918 Assessment of Fully Polarimetric ALOSPALSAR Data for Discriminating Wet  
919 Snow From Other Scattering Types in Mountainous Regions. *IEEE Trans.*  
920 *Geosci. Remote Sens.*, *52*, 1177–1196. doi:10.1109/TGRS.2013.2248369.
- 921 Singh, G., Verma, A., Kumar, S., Snehamani, Ganju, A., Yamaguchi, Y., &  
922 Kulkarni, A. V. (2017). Snowpack Density Retrieval Using Fully Polarimetric  
923 TerraSAR-X Data in the Himalayas. *IEEE Trans. Geosci. Remote Sens.*, *55*,  
924 6320–6329. doi:10.1109/TGRS.2017.2725979.

- 925 Snehmani, Venkataraman, G., Nigam, A. K., & Singh, G. (2010). Development  
926 of an inversion algorithm for dry snow density estimation and its application  
927 with ENVISAT-ASAR dual co-polarization data. *Geocarto Int.*, *25*, 597–616.  
928 doi:[10.1080/10106049.2010.516843](https://doi.org/10.1080/10106049.2010.516843).
- 929 Speziali, F., Trampuz, C., Placidi, S., Hendriks, L. C. I., Ludwig, M., & Meta, A.  
930 (2018). Development of the Multichannel Interferometric Ka-Band Airborne  
931 SAR Instrument (KaSAR). In *EUSAR 2018; 12th Eur. Conf. Synth. Aperture*  
932 *Radar* (pp. 1–5). Aachen, Germany. URL: [https://ieeexplore.ieee.org/  
933 abstract/document/8438262](https://ieeexplore.ieee.org/abstract/document/8438262).
- 934 Takala, M., Luojus, K., Pulliainen, J., Derksen, C., Lemmetyinen, J., Kärnä,  
935 J.-P., Koskinen, J., & Bojkov, B. (2011). Estimating northern hemisphere  
936 snow water equivalent for climate research through assimilation of space-borne  
937 radiometer data and ground-based measurements. *Remote Sens. Environ.*,  
938 *115*, 3517–3529. doi:[10.1016/j.rse.2011.08.014](https://doi.org/10.1016/j.rse.2011.08.014).
- 939 Tedesco, M. (Ed.) (2015). *Remote Sensing of the Cryosphere*. Chichester, UK:  
940 John Wiley & Sons, Ltd. doi:[10.1002/9781118368909](https://doi.org/10.1002/9781118368909).
- 941 Thakur, P. K., Aggarwal, S., Garg, P., Garg, R., Mani, S., Pandit, A., & Kumar,  
942 S. (2012). Snow physical parameters estimation using space-based Synthetic  
943 Aperture Radar. *Geocarto Int.*, *27*, 263–288. doi:[10.1080/10106049.2012.  
944 672477](https://doi.org/10.1080/10106049.2012.672477).
- 945 Thakur, P. K., Aggarwal, S. P., Arun, G., Sood, S., Senthil Kumar, A., Mani,  
946 S., & Dobhal, D. P. (2017). Estimation of Snow Cover Area, Snow Physical  
947 Properties and Glacier Classification in Parts of Western Himalayas Using  
948 C-Band SAR Data. *J. Indian Soc. Remote Sens.*, *45*, 525–539. doi:[10.1007/  
949 s12524-016-0609-y](https://doi.org/10.1007/s12524-016-0609-y).
- 950 Tridon, D. B., Sica, F., De Zan, F., Bachmann, M., & Krieger, G.  
951 (2018). Observation Strategy and Flight Configuration for Monitoring Earth  
952 Dynamics with the Tandem-L Mission. In *IGARSS 2018 - 2018 IEEE*



- 953 *International Geoscience and Remote Sensing Symposium* (pp. 5651–5654).  
954 doi:[10.1109/IGARSS.2018.8517757](https://doi.org/10.1109/IGARSS.2018.8517757).
- 955 Ulaby, F., Stiles, W., Dellwig, L., & Hanson, B. (1977). Experiments on the  
956 Radar Backscatter of Snow. *IEEE Trans. Geosci. Electron.*, *15*, 185–189.  
957 doi:[10.1109/TGE.1977.294490](https://doi.org/10.1109/TGE.1977.294490).
- 958 Usami, N., Muhuri, A., Bhattacharya, A., & Hirose, A. (2016). PolSAR Wet  
959 Snow Mapping With Incidence Angle Information. *IEEE Geosci. Remote*  
960 *Sens. Lett.*, *13*, 2029–2033. doi:[10.1109/LGRS.2016.2621891](https://doi.org/10.1109/LGRS.2016.2621891).
- 961 Wu, S., Li, J., & Huang, G. H. (2008). A study on DEM-derived primary  
962 topographic attributes for hydrologic applications: Sensitivity to elevation  
963 data resolution. *Appl. Geogr.*, *28*, 210–223. doi:[10.1016/j.apgeog.2008.](https://doi.org/10.1016/j.apgeog.2008.02.006)  
964 [02.006](https://doi.org/10.1016/j.apgeog.2008.02.006).
- 965 Yueh, S., Dinardo, S., Akgiray, A., West, R., Cline, D., & Elder, K. (2009).  
966 Airborne Ku-Band Polarimetric Radar Remote Sensing of Terrestrial Snow  
967 Cover. *IEEE Trans. Geosci. Remote Sens.*, *47*, 3347–3364. doi:[10.1109/](https://doi.org/10.1109/TGRS.2009.2022945)  
968 [TGRS.2009.2022945](https://doi.org/10.1109/TGRS.2009.2022945).
- 969 Zhu, Z., Wang, S., & Woodcock, C. E. (2015). Improvement and expansion of  
970 the Fmask algorithm: cloud, cloud shadow, and snow detection for Landsats  
971 47, 8, and Sentinel 2 images. *Remote Sens. Environ.*, *159*, 269–277. doi:[10.](https://doi.org/10.1016/j.rse.2014.12.014)  
972 [1016/j.rse.2014.12.014](https://doi.org/10.1016/j.rse.2014.12.014).
- 973 Zuniga, M., Habashy, T., & Kong, J. (1979). Active Remote Sensing of Layered  
974 Random Media. *IEEE Trans. Geosci. Electron.*, *17*, 296–302. doi:[10.1109/](https://doi.org/10.1109/TGE.1979.294658)  
975 [TGE.1979.294658](https://doi.org/10.1109/TGE.1979.294658).